Research Square

Preprints are preliminary reports that have not undergone peer review.
They should not be considered conclusive, used to inform clinical practice,
or referenced by the media as validated information.

Integrative transcriptomics identifies lncRNAs associated with trehalose transporter expression and carbohydrate homeostasis in Spodoptera frugiperda

Vikram Nichit
CSIR-National Chemical Laboratory
Vitthal T. Barvkar
Savitribai Phule Pune University
Rakesh S. Joshi
rs.joshi.ncl@csir.res.in

CSIR-National Chemical Laboratory

Research Article

Keywords: Long non-coding RNA, Trehalose, Transporter, Spodoptera frugiperda

Posted Date: November 12th, 2026

DOI: https://doi.org/10.21203/rs.3.rs-11082352/v1

License: This work is licensed under a Creative Commons Attribution 4.0 International License.
Read Full License

Additional Declarations: No competing interests reported.

Integrative transcriptomics identifies lncRNAs associated with trehalose transporter expression and carbohydrate homeostasis in *Spodoptera frugiperda*

Vikram Nichit [1,2], Vitthal T. Barvkar [3], Rakesh Joshi [1,2,*]

[1]Biochemical Sciences Division, CSIR-National Chemical Laboratory, Dr. Homi Bhabha Road, Pune, 411008, Maharashtra, India

[2] Academy of Scientific and Innovative Research (AcSIR), Ghaziabad 201002, Uttar Pradesh, India

[3] Department of Botany, Savitribai Phule Pune University, Ganeshkhind Road, Pune, Maharashtra 411007, India

***Corresponding author**

Dr. Rakesh S. Joshi,

Biochemical Sciences Division, CSIR – National Chemical Laboratory,

Dr. Homi Bhabha Road, Pashan, Pune – 411 008, India

Email: rs.joshi.ncl@csir.res.in

Tel (office): 020-2590-2247

Abstract:

Trehalose metabolism is a key component of insect physiological homeostasis, yet its regulation by long non-coding RNAs (lncRNAs) remains poorly understood. To characterize the lncRNAs associated with trehalose metabolism, we analysed *Spodoptera frugiperda* transcriptomes in trehalose-6-phosphate synthase (*SfTPS*) and trehalase (*SfTreh*) silenced, together with glucose- and trehalose-feeding treatments. Sequence-structure analysis, along with co-expression network analysis identified hub lncRNAs associated with protein coding transcripts. Functional annotations of co-expressed mRNAs highlighted *SfTRET* as one of the key regulatory targets. Co-expression, genomic localization, expression correlation and RNA-RNA interaction prediction integration prioritized key candidates of lncRNA-*SfTRET* association. Silencing of selected lncRNAs deregulates *SfTRET1* expression and larval growth. Altered accumulation of trehalose metabolism related metabolites was observed following candidate lncRNA silencing. Collectively, these findings identify candidate lncRNAs associated with *SfTRET1* expression, trehalose homeostasis, and larval growth in *S. frugiperda*, providing an integrative framework for understanding lncRNA-associated regulation of insect carbohydrate metabolism.

Keywords:

Long non-coding RNA, Trehalose, Transporter, *Spodoptera frugiperda*

Introduction

Trehalose is the major circulating sugar in insect haemolymph and functions as both an immediately mobilizable energy reserve and stress protectant (Tang et al. 2018; Huang et al. 2021; Tellis et al. 2023). Trehalose can constitute approximately 90% of the circulating haemolymph sugar, underscoring its central role in systemic energy allocation during growth, molting, flight, diapause, and stress adaptation (Tang et al. 2018; Wang et al. 2021; Huang et al. 2021; Yang et al. 2024). Trehalose is synthesised primarily via the trehalose-6-phosphate synthase/trehalose-6-phosphate phosphatase (TPS/TPP) pathway and is subsequently hydrolysed by trehalase (TREH), releasing glucose for cellular energy production. Trehalose is transported from its site of biosynthesis, the fat body, to energy-demanding tissues like muscle, reproductive organ and brain through trehalose transporters (TRETs). Across insect species, functional perturbation studies consistently show that TPS and TREH genes form a metabolic-developmental axis linking carbohydrate balance to chitin homeostasis, molting success, and fitness. TPS or TREH silencing leads to abnormal phenotypes, lethality or delayed development, altered trehalose and glucose content, reduced chitin synthesis, and dysregulation of chitin-pathway genes in *Leptinotarsa decemlineata*, *Acyrthosiphon pisum*, *Nilaparvata lugens*, *Mythimna separata*, *Frankliniella occidentalis*, and *Hyphantria cunea* (Shi et al. 2016; Wang et al. 2021; Zhou et al. 2022; Yang et al. 2023; Zheng et al. 2024; Wu et al. 2025).

In *Spodoptera frugiperda (S. frugiperda)*, one of the most destructive agricultural pests worldwide, trehalose metabolism is increasingly recognized as an important determinant of carbohydrate homeostasis, development, reproduction, and adaptation to environmental stress. RNAi-mediated suppression of trehalose biosynthesis and degradation disrupts the trehalose-glucose balance and adversely affects larval survival and development, demonstrating the physiological importance of maintaining trehalose homeostasis (Yang et al. 2024). Pharmacological inhibition or RNAi-mediated suppression of trehalase disrupts trehalose utilization and carbohydrate homeostasis, resulting in developmental abnormalities, altered physiological performance, and reduced survival under environmental stress, highlighting the importance of regulated trehalose metabolism in *S. frugiperda* (Zhong et al. 2023; Barbole et al. 2024; Gokulanathan et al. 2024).

Broader regulatory analyses further indicate that trehalose metabolism is governed by tissue-specific gene expression, substrate availability, feedback

regulation by pathway intermediates and products, and neuroendocrine control coordinating trehalose production, uptake, and degradation according to nutritional and developmental state (Tellis et al. 2023). Although the protein-coding enzymes of this pathway have been increasingly characterized, the upstream regulatory logic that coordinates trehalose synthesis, hydrolysis, transport, and developmental deployment remains incompletely resolved (Tang et al. 2018; Tellis et al. 2023). Current models indicate that transcription factors, endocrine signals, pathway feedback, and tissue-specific dynamics shape trehalose metabolism (Tellis et al. 2023; Mohite et al. 2026). This makes it plausible that non-coding regulators fine-tune the pathway, particularly under developmental or nutritional perturbation.

Long non-coding RNAs (lncRNAs) are a strong candidate regulatory layer in this context because insect ncRNA research increasingly shows that non-coding transcripts participate in post-transcriptional and network-level control of complex phenotypes (Muthu Lakshmi Bavithra et al. 2023; Xiao et al. 2024). LncRNAs are generally defined as transcripts longer than 200 nucleotides with no protein-coding potential and can regulate gene expression through diverse mechanisms, including chromatin remodelling, transcriptional regulation, RNA processing, transcript stability, and interactions with proteins. In insects, lncRNAs have been implicated in detoxification, cuticle-associated responses, and insecticide resistance, and can act through broader ceRNA-like regulatory networks involving miRNAs and metabolic effector genes (Rahman et al. 2024; Xiao et al. 2024; Meng et al. 2025). Genome-wide analyses have revealed large and functionally diverse lncRNA repertoires in insects, including 8,394 lncRNAs in *Helicoverpa armigera*, with hundreds associated with detoxification-related functions, and thousands of lncRNAs in *Tribolium castaneum* associated with metabolic processes such as glycolysis, the tricarboxylic acid cycle, and amino-acid metabolism, suggesting broader roles for insect lncRNAs in detoxification and cellular energy homeostasis (Yang et al. 2021; Rahman et al. 2024). Furthermore, accumulating evidence has implicated lncRNAs in development, immunity, environmental adaptation, and insecticide resistance (Satyavathi et al. 2017; Xiao et al. 2024). Taken together, these findings support the broader hypothesis that lncRNAs can integrate physiological state with gene expression programs relevant to metabolism, development, and adaptation, even though their role in trehalose homeostasis, and especially in the regulation of trehalose transport, remains largely unexplored in *S. frugiperda*.

In the present study, we performed an integrative transcriptomic analysis to investigate lncRNAs associated with trehalose metabolism in *S. frugiperda* under RNAi-mediated silencing of trehalose pathway genes and glucose- and trehalose-feeding conditions. By combining high-throughput RNA sequencing, differential expression analysis, secondary structure stability prediction, genomic characterization, and coexpression network analysis, we identified high-confidence lncRNAs potentially involved in carbohydrate metabolism, especially the TRET. Candidate lncRNAs showing co-expression with *TRET* were further functionally evaluated by RNAi-mediated silencing to examine their effects on *TRET* expression and insect development. This study provides new insights into lncRNA-mediated regulation of trehalose metabolism and establishes a foundation for future investigations into RNA-based strategies for sustainable management of *S. frugiperda*.

Materials and Methods

RNA-Seq datasets

The RNA-seq datasets analyzed in this study were generated as part of independent experiments conducted in our laboratory and are publicly available in the NCBI Sequence Read Archive (SRA). Two transcriptome datasets were analyzed: (i) an RNA interference (RNAi) dataset comprising *Spodoptera frugiperda* larvae subjected to dsRNA-mediated silencing of *SfTPS* and *SfTreh*, together with their respective L4440 control groups, and (ii) a sugar-feeding dataset comprising larvae fed glucose, trehalose, or an artificial diet as the control. Total RNA was isolated from each treatment group, and paired-end RNA sequencing libraries were prepared and sequenced on the Illumina platform. The resulting raw sequencing reads were used as the input for all downstream bioinformatic analyses performed in the present study.

RNA-seq data processing and transcriptome reconstruction

Raw paired-end RNA-seq reads of ds*SfTPS*-ds*SfTreh* and sugar-fed (glucose and trehalose) transcriptome were first subjected to quality assessment using FastQC (Andrews et al. 2010) to evaluate per-base sequence quality, GC content, adapter contamination, and duplication levels. Adapter sequences and low-quality bases were removed using Trim Galore (v0.6.10) (Krueger et al. 2023), generating high-quality trimmed reads for downstream analysis.

Clean reads were aligned to the *Spodoptera frugiperda* reference genome (GCF_023101765.2) using the splice-aware aligner HISAT2 (v2.2.1) (Kim et al. 2019). Genome indices were constructed using exon and splice-site information extracted from the corresponding genome annotation to facilitate accurate alignment across exon-exon junctions. The resulting alignments were sorted and converted into BAM format for each sample for downstream transcript assembly.

Reference-guided transcript assembly and expression quantification were performed using StringTie v2.1.4 (Pertea et al. 2015) following the HISAT-StringTie transcriptome reconstruction framework (Pertea et al. 2016). Sample-specific assemblies were merged to generate a unified transcript annotation set, which was subsequently used for re-quantification across all samples. Gene- and transcript-level expression matrices were generated using the prepDE.py script from the StringTie package, producing count tables suitable for downstream statistical and differential expression analyses in R.

Identification of lncRNAs from *Spodoptera frugiperda* ds*SfTPS*–ds*SfTreh* and sugar-fed transcriptome

Long noncoding RNAs (lncRNAs) were identified from the *Spodoptera frugiperda* ds*SfTPS*–ds*SfTreh* and sugar fed (glucose and trehalose) transcriptomes using a stringent multi-step computational pipeline. Transcript sequences were extracted from the assembled GTF file using gffread with the corresponding *S. frugiperda* reference genome (Pertea and Pertea 2020). To obtain high-confidence candidates, transcripts were filtered to retain only those with ≥2 exons and a minimum length of ≥200 bp using SeqKit (Shen et al. 2016). Coding potential of the filtered transcripts was evaluated using three independent tools: the deep learning-based lncRNA_Mdeep (Fan et al. 2020), the support vector machine-based CPC2 (Kang et al. 2017), and the intrinsic sequence composition-based CNCI (Sun et al. 2013). Only transcripts consistently classified as noncoding by all three approaches were retained as candidate lncRNAs.

Potential protein-coding contamination were further excluded by searching candidate sequences against the curated UniProt Swiss-Prot database using DIAMOND (Buchfink et al. 2015) with an E-value cutoff of $<1 \times 10^{-5}$. Known structural and housekeeping RNA contaminants such as rRNA and tRNA were removed by performing covariance model searches using Infernal cmscan against the Rfam

database (Nawrocki and Eddy 2013; Kalvari et al. 2021) with an E-value threshold of <1 x 10^{-5}. To identify and remove potential protein-coding transcripts from the high-confidence lncRNA dataset, predicted open reading frames (ORFs) were generated from the lncRNA sequences using TransDecoder (Haas et al. 2013), producing putative protein sequences. These proteins were then scanned against the Pfam-A database (Mistry et al. 2021) using hmmscan (Eddy 2011) to detect conserved protein domains. Transcripts with significant Pfam domain hits (independent E-value ≤ 1 x 10^{-3}) were considered likely protein-coding and were extracted from the Pfam output. These putative coding transcripts were subsequently removed from the original lncRNA set using SeqKit. The resulting transcripts were retained as high-confidence lncRNAs for downstream analyses. Expression profiles of the identified lncRNAs were obtained by matching their transcript IDs to the corresponding transcript-level count matrices.

Differential expression analysis of lncRNAs and protein-coding genes

Differential expression analyses were performed independently for high-confidence lncRNAs and protein-coding genes within the ds*SfTPS*/ds*SfTreh* RNAi and sugar-fed (glucose and trehalose) transcriptomes. Raw transcript- and gene-level count matrices, respectively, were analysed using DESeq2 (version 1.42.0) in R (Love et al. 2014). Low-abundance features were removed by retaining lncRNAs or genes with a total raw count >10 across all samples within the corresponding dataset. DESeq2 normalization, dispersion estimation, and differential expression testing were performed using DESeq() with a design formula of ~ condition.

Pairwise comparisons comprised ds*SfTPS* vs control, ds*SfTreh* vs control, and ds*SfTPS* vs ds*SfTreh* for the RNAi transcriptome, and glucose vs control, trehalose vs control, and glucose vs trehalose for the sugar-fed transcriptome. Log2 fold-change estimates for both lncRNAs and protein-coding genes were stabilized using the apeglm method implemented through lfcShrink() (Zhu et al. 2019), *P* values were adjusted for multiple testing using the Benjamini–Hochberg false discovery rate procedure (Benjamini and Hochberg 1995). lncRNAs and protein-coding genes with an adjusted $P \leq 0.05$ and |log2 fold change| >1 were considered differentially expressed.

Expression patterns of differentially expressed lncRNAs and protein-coding genes were visualized using variance-stabilizing transformation (VST)-normalized expression values, followed by row-wise Z-score scaling and hierarchical clustering using Euclidean distance and complete linkage in ComplexHeatmap (Gu et al. 2016). Volcano plots were generated using ggplot2 (Wickham 2016). Shared and comparison-specific differentially expressed features within each transcriptome were visualized using VennDiagram (Chen and Boutros 2011), whereas intersections across multiple comparisons were examined using UpSet plots generated with ComplexUpset (Gu et al. 2016).

Exon-number distributions of high-confidence lncRNAs were determined independently for the ds*SfTPS*–ds*SfTreh* RNAi and sugar-fed transcriptomes using their corresponding StringTie-assembled GTF annotations. Exon features associated with each lncRNA were extracted and counted per transcript. lncRNAs were classified into five groups containing 2, 3, 4, 5, or ≥6 exons, and their distributions were compared between transcriptomes.

Prediction of lncRNA subcellular localization

The subcellular localization of candidate lncRNAs was predicted using lncLocator (Cao et al. 2018), a machine learning-based predictor for lncRNA localization. The nucleotide sequences of lncRNAs were used as input, and localization probabilities were determined for the nucleus, cytoplasm, ribosome, cytosol, and exosome. The compartment with the highest probability score was assigned as the final localization site of each lncRNA. The distribution of lncRNAs among different cellular compartments was visualized using ggplot2 in R (version 4.4.2).

Structural stability analysis of lncRNAs

A total of 114 differentially expressed (DE) lncRNAs, comprising 100 from the ds*SfTPS*–ds*SfTreh* RNAi transcriptome and 14 from the sugar-fed transcriptome, were subjected to secondary structure analysis. RNA secondary structures and thermodynamic parameters were predicted using RNAfold implemented in ViennaRNA package (version 2.7.2)(Lorenz et al. 2011). Partition function calculations were performed using *RNAfold -p -d2 –noLP* to obtain minimum free energy (MFE;

kcal/mol), ensemble free energy (kcal/mol), centroid free energy (kcal/mol), MFE frequency (%), and ensemble diversity. As thermodynamic parameters are inherently dependent on transcript length, all energy values were normalized by sequence length (in nucleotides) to enable accurate cross-transcript comparisons. The normalized metrics calculated included MFE_norm (kcal/mol/nt), Ensemble_norm (kcal/mol/nt), Centroid_norm (kcal/mol/nt), and Diversity_norm (per nucleotide). Additionally, the Energy_gap was computed as the difference between Ensemble Free Energy and MFE, representing the thermodynamic separation between the most stable structure and the ensemble average. To classify structurally stable lncRNAs, a two-dimensional stability framework was constructed by plotting MFE_norm against Diversity_norm. This integrative approach enabled simultaneous evaluation of thermodynamic stability and conformational variability. Transcripts exhibiting highly negative MFE_norm values along with low Diversity_norm values clustered in the lower-left quadrant of the plot and were considered structurally stable candidates. Threshold cutoffs of ≤ −0.2 kcal/mol/nt for MFE_norm and ≤ 0.2 per nucleotide for Diversity_norm were applied to define strong thermodynamic stability and low structural diversity. lncRNAs satisfying both criteria were classified as possessing stable and dominant secondary structures.

Pseudoknot prediction and structural refinement

Pseudoknot-containing secondary structures of structurally stable lncRNAs were predicted using IPknot++ (Version 2.3.1) (Sato and Kato 2022), which predicts maximum expected accuracy (MEA) RNA secondary structures including pseudoknots based on base-pairing probabilities (Sato et al. 2011). To address length-dependent computational complexity, two models were applied: lncRNAs ≤500 nt were analyzed using the McCaskill partition function with ViennaRNA parameters, while lncRNAs >500 nt were processed using the LinearPartition-V (lpv) model (Zhang et al. 2020) with ViennaRNA parameters for efficient approximation of partition functions in long sequences.

In the IPknot++ output, pseudoknot interactions are denoted by square brackets (“[” and “]”). The total number of pseudoknot base pairs per transcript was determined by counting the number of opening brackets (“[”), each representing one pseudoknot interaction. To eliminate transcript length bias, pseudoknot density was calculated as the number of pseudoknot base pairs divided by transcript length (nt), providing a

normalized measure of structural enrichment. Only structurally stable, coding-validated lncRNAs predicted to contain pseudoknot interactions were retained for downstream analyses.

Co-expression network construction

To investigate the regulatory relationships between long non-coding RNAs (lncRNAs) and protein-coding genes, co-expression network analysis was performed using the sugar-fed and the ds*SfTPS*_ds*SfTreh RNAi* transcriptome. Differentially expressed stable lncRNAs and protein-coding genes (DEGs) identified from each dataset were used for the analysis. Variance stabilizing transformation (VST)-normalized expression matrices generated using DESeq2 were imported into R. Only samples common to both the lncRNA and mRNA expression matrices were retained, and transcripts containing missing values were excluded before downstream analysis. Pairwise Pearson correlation analysis was performed between each lncRNA and mRNA using the cor.test() function in R with the Pearson correlation method. For every lncRNA–mRNA pair, the Pearson correlation coefficient (r) and the corresponding P-value were calculated. Significant co-expression relationships were defined as those with an absolute Pearson correlation coefficient ($|r|$) ≥ 0.9 and $P < 0.05$. The resulting significant lncRNA–mRNA pairs were retained for construction of the co-expression networks. The significant co-expression pairs were ranked according to the absolute correlation coefficient, and hub lncRNAs were identified by calculating the degree of each lncRNA, defined as the number of significantly correlated mRNAs. The resulting co-expression networks and hub degree tables were exported for downstream network visualization and hub analysis. The lncRNA–mRNA co-expression network was visualized using the igraph, ggraph, and ggplot2 packages in R. Significant lncRNA–mRNA co-expression pairs identified from the transcriptome analysis were imported as an edge list, with lncRNAs and mRNAs represented as nodes and significant correlations represented as edges. Duplicate interactions were removed before network construction. Edge colors represented the direction of the correlation, with green indicating positive correlations and red indicating negative correlations, while edge widths were scaled according to the absolute correlation coefficient. Node connectivity (degree) was calculated using the igraph package to identify highly connected hub lncRNAs. Node sizes were

proportional to connectivity for lncRNAs, whereas mRNAs were displayed using a constant node size to improve visualization. To reduce visual complexity, only the top 40 hub lncRNAs ranked by node degree were labelled. In addition, node degree values for all lncRNAs and mRNAs were calculated and exported to identify candidate hub lncRNAs for downstream functional analyses.

Functional annotation of lncRNA-associated protein-coding genes

To characterize the potential functions of structurally stable DE lncRNAs, Gene Ontology (GO) annotations were examined for their co-expressed protein-coding genes from the ds*SfTPS*–ds*SfTreh* RNAi and sugar-fed transcriptomes. Significant lncRNA–mRNA associations were identified from Pearson correlation-based co-expression networks using $|r| \geq 0.90$ and $P < 0.05$. Functional annotation was performed using OmicsBox v3.4. Protein sequences were searched against the NCBI non-redundant (nr) protein database using BLASTp (Altschul et al. 1990) with an E-value threshold of 1 × 10^−3 to identify putative homologues. Protein domains and families were characterized using InterProScan v5.74-105.0 (Jones et al. 2014). Gene Ontology (GO)(Gotz et al. 2008) terms were assigned by integrating BLAST-based GO mapping with InterProScan-derived annotations and were classified into the three major GO categories: biological process, molecular function, and cellular component. Redundant and low-frequency terms were removed, and the numbers of upregulated and downregulated genes assigned to each GO term were summarized separately for the RNAi and sugar-fed transcriptomes. GO functional profiles were visualized as butterfly bar plots.

Prediction of lncRNA–mRNA Interactions

Candidate lncRNA–mRNA interactions were evaluated using IntaRNA v3.4.1, which predicts RNA–RNA interactions by integrating sequence complementarity, hybridization energetics, and interaction-site accessibility (Mann et al. 2017). Candidate pairs were selected from the lncRNA–mRNA co-expression networks based on significant expression correlations and network connectivity. Full-length sequences of selected hub lncRNAs were extracted from the assembled transcriptomes and used as query sequences. Corresponding target transcripts were retrieved using the reference genome annotation, with LOC identifiers mapped to their

respective RefSeq mRNA (XM) or non-coding RNA (XR) accessions, while novel StringTie transcripts (MSTRG IDs) were retained directly.

Each candidate lncRNA was analyzed against its corresponding target transcript(s) using IntaRNA with default parameters. Predicted interactions were characterized based on interaction energy, hybridization energetics, interaction coordinates, and complementary regions. More negative interaction energies were interpreted as indicating thermodynamically more favorable predicted interactions. IntaRNA predictions were subsequently integrated with co-expression and network-connectivity information to prioritize high-confidence candidate lncRNA–mRNA interaction pairs for downstream analyses.

Cross-validation of lncRNA–mRNA interactions using RNAcofold and RNAup

Candidate lncRNAs predicted to interact with trehalose transporter transcripts (*SfTRET1*; LOC118277428, LOC118270239, and LOC126911554) were prioritized by integrating differential expression, functional annotation, co-expression, and IntaRNA interaction predictions. RNA–RNA interactions were independently assessed using RNAcofold (Bernhart et al. 2006; Lorenz et al. 2011) and RNAup (Mückstein et al. 2006) implemented in the ViennaRNA Package (v2.7.0). RNAcofold was used to predict the thermodynamically optimal joint secondary structure of each lncRNA–mRNA pair and estimate the minimum free energy (MFE) of heterodimer formation. RNAcofold is specifically designed to calculate secondary structures of two interacting RNA molecules with dimerization.

RNAup was used to estimate interaction free energy by considering both the energetic cost of making the interacting regions accessible and the energy gained through intermolecular hybridization. Predicted interaction energies, binding coordinates, and interacting regions obtained using RNAcofold and RNAup were compared with the corresponding IntaRNA predictions. Candidate lncRNA–mRNA pairs showing favorable interaction energies and concordant or overlapping binding regions across multiple algorithms were considered higher-confidence computational interaction candidates for subsequent functional validation.

Genomic cis–trans classification of candidate lncRNA–mRNA interactions

To determine the genomic relationship between candidate lncRNAs and their predicted target genes, genomic coordinates were extracted from the StringTie merged GTF annotation of the ds*SfTPS*–ds*SfTreh* RNAi and sugar-fed transcriptomes. Chromosome, strand, transcript start, and end coordinates were retrieved for the three *SfTRET1*-associated target loci (*LOC118277428*, *LOC118270239*, and *LOC126911554*) and their corresponding candidate lncRNAs. The genomic positions of each lncRNA–mRNA pair were compared to assess whether they were located on the same chromosome (cis) or on different chromosomes (trans). For lncRNAs located on the same chromosome as their target gene, the genomic distance was evaluated to determine whether they fell within a conventional cis-regulatory window.

Genomic classification, chromosomal distribution, and length distribution analysis of lncRNAs

The genomic characteristics of the 2,589 and 2,636 high-confidence lncRNAs identified from the ds*SfTPS*–ds*SfTreh*RNAi and sugar-fed transcriptomes, respectively, were evaluated. Genomic locations were determined by comparing the final lncRNA annotations with a protein-coding reference GTF using GffCompare (Pertea and Pertea 2020). Based on GffCompare class codes, lncRNAs were categorized as intergenic (u), intronic (i), antisense (x), same-strand exonic overlap (o), or other transcript–reference relationships (=, j, k, y, n, and s). Chromosomal distribution was determined from genomic coordinates by calculating the number of lncRNAs mapped to each chromosome or scaffold. Transcript lengths were calculated from the final annotations and grouped into 200–500, 501–1,000, 1,001–2,000, and >2,000 bp classes. Genomic-location, chromosomal-distribution, and transcript-length profiles were visualized using ggplot2 in R.

Insect culture

S. frugiperda eggs were obtained from the ICAR–National Bureau of Agricultural Insect Resources (ICAR-NBAIR), Bengaluru, India. After hatching, larvae were reared on a chickpea-based artificial diet (AD) (Chikate et al. 2016) at 28 °C, 80% relative humidity (RH), and a 16:8 h light:dark photoperiod. Second-generation insects were used for feeding and ‘-omics’ experiments.

RNAi-mediated silencing of candidate *SfTRET1*-associated lncRNAs by bacterial dsRNA feeding

Partial fragments of *lnc_XR007706201.1, lnc_MSTRG.4937.1* interacting with *SfTRET1* (LOC118277428) and *lnc_XR_007705431.1* interacting with *SfTRET1* (LOC126911554) were cloned into the L4440 vector for RNAi using gene-specific primers, and the resulting constructs were confirmed by sequencing **(Table S3)**. The resulting recombinant vectors (L4440- *lnc_XR007706201.1*; L4440- *lnc_MSTRG.4937.1* and L4440- *lnc_XR_007705431.1*), and the L4440-GFP, were transformed into *E. coli* HT115 (DE3) cells. To prepare the bacteria expressing dsRNA, a single colony was inoculated into Luria-Bertani (LB) broth supplemented with 100 µg/mL ampicillin and 12.5 mg/mL tetracycline antibiotics and incubated for 14 hours at 37°C with agitation at 180 rpm. The culture was then diluted 100-fold in 250 mL yeast tryptone (2xYT) medium and grown at 37°C with agitation at 180 rpm, with appropriate antibiotics, until the optical density (OD) reached 0.4. The synthesis of dsRNAs was induced by adding 1 mM isopropyl β-D-1-thiogalactopyranoside (IPTG), and these cultures were incubated for 5 hours under similar conditions. Bacterial cells were then pelleted by centrifugation at 4000 rpm at 4°C. Confirmation of dsRNA expression was achieved by extracting total RNA from aliquots of induced and uninduced culture using TRIzol reagent (TaKaRa Bio, Shiga, Japan) according to the manufacturer's instructions, and dsRNAs were visualized on a 2% agarose gel.

Feeding bioassay of *lnc_XR007706201.1*-dsRNA, *lnc_MSTRG.4937.1*-dsRNA and *lnc_XR_007705431.1*-dsRNA expressing bacteria to *S. frugiperda*

Bacterial cultures of dsRNA targeting *lnc_XR007706201.1*, *lnc_MSTRG.4937.1, lnc_XR_007705431.1* and L4440-GFP control were used for feeding second-instar *S. frugiperda* larvae, respectively. IPTG-induced 250 mL bacterial cultures were centrifuged at 4000 rpm for 10 minutes at 4°C, then resuspended in 4 mL of DEPC water. AD was prepared according to the methodology described by Chikate et al. Bacterial cultures were then added to the AD at a final optical density (OD) of 1. Feeding bioassays were conducted on second instar larvae of *S. frugiperda*, with 19 larvae per treatment. The larvae were fed either an artificial diet containing L4440-GFP vector bacterial culture (Control) or bacterial cultures expressing L4440-*lnc_XR007706201.1*-dsRNA, L4440-*lnc_MSTRG.4937.1*-dsRNA and L4440-

lnc_XR_007705431.1-dsRNA. Insect growth and survival on both the control and dsRNA-containing diets were monitored on alternate days until pupation. On day 6, seven larvae from each treatment were collected and immediately frozen in liquid nitrogen for molecular analysis, with individual larvae treated as independent biological replicates. Silencing efficiency of *lnc_XR007706201.1*, *lnc_MSTRG.4937.1,* and *lnc_XR_007705431.1* was evaluated by qRT-PCR.

RNA extraction and quantitative reverse-transcriptase PCR (qRT-PCR) analysis

Total RNA was isolated from *S. frugiperda* using RNAiso Plus reagent (TaKaRa, Shiga, Japan) according to the manufacturer's instructions, followed by DNase treatment with RQ1 RNase-free DNase (Promega, Madison, USA) to remove genomic DNA contamination. First-strand cDNA was synthesized from 4 µg of total RNA using oligo(dT) primers and the High-Capacity cDNA Reverse Transcription Kit (Applied Biosystems, Foster City, USA). Quantitative real-time PCR (qRT-PCR) was performed using TB Green Premix Ex Taq II (TaKaRa, Shiga, Japan) on a 7500 Fast Real-Time PCR System (Applied Biosystems, Foster City, USA), with gene-specific primers designed using Primer-BLAST (NCBI) (**Table S3**). The thermal cycling conditions consisted of an initial denaturation at 95°C for 30 second, followed by 40 cycles of 95°C for 5 second and 55°C for 30 second, along with melt curve analysis to confirm specificity. Relative expression levels of *SfTRET1 and lncRNAs* were quantified using relative gene expression 2^(-ΔΔCt) method. *S. frugiperda* ribosomal protein L (*SfRPL3*) used as internal reference gene. All qRT-PCR assays were performed using three biological replicates, with three technical replicates for each biological replicate.

Metabolite extraction and LC–MS analysis

Individual insects were considered independent biological replicates, with one insect representing one biological replicate. For metabolite extraction, 60 mg of crushed insect tissue was homogenized in 300 µL of 80% methanol (v/v). The homogenate was vortexed for 1 min, followed by bath sonication for 30 min in ice-cold water, and centrifuged at 14,000 × g for 30 min. The resulting supernatant was collected and stored at −80 °C overnight to facilitate protein precipitation. Samples were subsequently centrifuged again at 14,000 × g for 30 min, and the clarified supernatant was passed through a 0.22-µm syringe filter. The filtrate was transferred into LC–MS

sample vials for subsequent metabolomic analysis. The Hypersil GOLD (150 × 2.1 mm, 1.9 µm particle size) (Thermo Fisher Scientific, Vilnius, Lithuania) column was used for UPLC-based metabolite separation at 35 °C with a flow rate of 0.3 ml/min. The metabolites were separated using a 20 min gradient with 100% MS-grade water (Solvent A) and 100% MS-grade acetonitrile (Solvent B), both containing 0.1% formic acid. The LC-QTOF-MS analysis was performed on an Agilent 6530 Q-TOF (Agilent Technologies, Santa Clara, USA). For peak extraction, baseline filtering, calibration, peak alignment, deconvolution, peak identification, and integration, MS-DIAL software (Tsugawa et al. 2015) version 4.9.221218 (http://prime.psc.riken.jp/Metabolomics_Software/MS-DIAL/index.html) was utilized, with an LC–MS/MS spectral database sourced from MassBank of North America. Quantification of metabolites involved in glucose and energy metabolism was carried out. In this study, LC-HRMS peak intensities were normalized using a total peak height (or area) / total ion current (TIC) normalization approach**.** Briefly, normalization was performed at the sample level by dividing the intensity of each detected feature by the sum of all peak intensities within the same sample**.** This procedure scales each feature relative to the total signal contribution of that sample, correcting for variation in sample loading, ionization efficiency, and instrument response across injections (Mizuno et al. 2017). The following formula was used for normalization:

Normalized peak intensity = Peak height (or area) / Total ion current (TIC)

Statistical analyses

Statistical analyses were performed using R and GraphPad Prism v8.0 (GraphPad Software, San Diego, CA, USA). Experimental data are presented as mean ± SEM. Biological replicates were treated as independent experimental units, whereas technical replicates from qRT-PCR assays were averaged before statistical analysis. For comparisons between two independent experimental groups, an unpaired two-tailed Student's *t*-test was used. Comparisons involving more than two groups were performed using one-way ANOVA followed by Tukey's multiple-comparisons test. Temporal changes in larval body weight were analysed using two-way repeated-measures ANOVA with treatment and time as factors, followed by Šídák's multiple-comparisons test for comparisons between treatment groups at individual time points. Pearson's correlation coefficient (*r*) was used to assess expression relationships

between candidate lncRNAs and *SfTRET1* transcripts. Differences in pseudoknot count and normalized pseudoknot density between datasets were assessed using a two-sided Wilcoxon rank-sum test. Differential expression analyses of lncRNAs and protein-coding genes were performed using DESeq2, with *P*-values corrected for multiple testing using the Benjamini–Hochberg procedure; transcripts with adjusted $P \leq 0.05$ and |log2 fold change| >1 were considered differentially expressed. For metabolomic analyses, normalized metabolite abundances were compared between experimental groups and $P < 0.05$ was considered statistically significant.

Declaration of generative AI-assisted technologies in the writing process

During the preparation of this work, the author(s) used ChatGPT and Grammarly to enhance readability. After using this tool/service, the author reviewed and edited the content as needed and take full responsibility for the content of the publication.

Results

Trehalose metabolic and dietary perturbations cause global changes in lncRNA landscape

A comprehensive pipeline was employed to identify high-confidence lncRNAs from the *S. frugiperda TPS* and *TREH* silenced transcriptome available with us **(Fig. 1a)**. A total of 416.18 million raw paired-end reads were generated from 12 ds*SfTPS* and *dsSfTreh* RNA-seq libraries, yielding an average of 34.68 million reads per library. The overall alignment rate ranged from 82.45 to 87.39%, with an average mapping rate of 85.98% **(Table S1)**. Following transcript reconstruction (46,346 initial transcripts), structural filtering retained 41,035 multi-exonic transcripts ≥200 bp. Coding potential assessment using lncRNA_Mdeep (4,897), CPC2 (4,547), and CNCI (7,112) yielded a consensus intersection of 3,271 putative non-coding candidates. To eliminate false positives, transcripts were sequentially filtered against UniProt Swiss-Prot via DIAMOND (removing 290 protein-coding matches), Rfam via Infernal cmscan (removing 63 housekeeping RNAs), and Pfam via HMMScan (removing 329 conserved protein domains). This multi-tier refinement pipeline resulted in a final high-confidence set of 2,589 lncRNAs for downstream analyses **(Fig. 1a)**.

Expression profiling across the *SfTPS* and *SfTreh* silencing transcriptome identified 100 differentially expressed lncRNAs (29 upregulated, 71 downregulated;

Table S1). Pairwise comparisons revealed distinct, condition-specific transcriptional dynamics. *SfTPS* silencing elicited a transcriptional response characterized predominantly by the downregulation of candidates such as *XR_007707652.1*, *MSTRG.12548.1*, and *MSTRG.10103.21* **(Fig. 1b)**, which resolved into a distinct repressed cluster upon hierarchical clustering **(Fig. 1c)**. Conversely, *SfTreh* knockdown produced a more pronounced transcriptional shift dominated by repressed transcripts, including *MSTRG.12532.1*, *XR_004783803.2*, *XR_007707620.1*, and *XR_004783195.2* **(Fig. 1d)**, cleanly partitioning treated and control cohorts **(Fig. 1e)**. The ds*SfTPS* vs ds*SfTreh* contrast exhibited the greatest transcriptional divergence, displaying widely dispersed fold changes **(Fig. 1f)** and reciprocal expression profiles **(Fig. 1g**), where *MSTRG.4937.1*, *MSTRG.4345.2*, and *MSTRG.6956.8* were strongly upregulated, and *XR_007706201.1*, *MSTRG.10987.5*, and *MSTRG.9440.11* were markedly downregulated. Cross-comparison intersection revealed largely distinct regulatory programs: 64 differentially expressed lncRNAs (67%) were specific to ds*SfTPS* vs ds*SfTreh*, 16 (17%) to ds*SfTreh* vs control, and 10 (11%) to ds*SfTPS* vs control, with zero transcripts shared across all three contrasts **(Fig. S1a)**. Consistent with characteristic non-coding transcript profiles, lncRNAs exhibited significantly lower steady-state expression levels than protein-coding mRNAs (median normalized counts: 0.85 vs 1.77; $P < 2.2 \times 10\text{-}16$, Wilcoxon rank-sum test; **Fig. S1b**). Among the 2,589 lncRNAs identified from the RNAi transcriptome, intergenic (1,003) and intronic (810) lncRNAs were predominant, followed by antisense (387), splice-junction-associated (156), same-strand exonic-overlap (99), and exact-reference-match (72) transcripts, while 62 belonged to other categories. The lncRNAs were distributed across all assembled chromosomes, with chromosome-wise abundance ranging from approximately 28 to 216 transcripts. Individual lncRNA lengths showed a broad distribution, with the majority concentrated around 1 kb and a smaller proportion extending beyond several kilobases **(Fig. 1h-j; Fig. S1c; Table S1)**.

In parallel with the knockdown approach, we next delineated lncRNA dynamics under dietary carbohydrate shifts (glucose vs trehalose supplementation) using an identical identification pipeline **(Fig. 2a).** High-throughput sequencing of nine sugar-fed libraries generated 166.57 million raw reads with an 83.90% mean mapping rate, yielding 46,070 reconstructed transcripts **(Table S1)**. Structural filtering (≥200 bp, multi-exonic; 39,732 transcripts), consensus non-coding prediction (MDeep, CPC2,

CNCI; 3,255 transcripts), and sequential depletion of Swiss-Prot protein matches (275), Rfam housekeeping RNAs (55), and Pfam domains (289) defined a final dataset of 2,636 high-confidence sugar-responsive lncRNAs **(Fig. 2a)**.

Expression analysis (adjusted $P \leq 0.05$ and $|\log_2$ fold change$| > 1$) identified 14 lncRNAs (9 upregulated, 5 downregulated; **Table S1**). In glucose-fed larvae, *MSTRG.2003.5* and *MSTRG.4316.8* were markedly induced, whereas *XR_007705429.1* and *XR_007705431.1* were significantly repressed relative to controls **(Fig. 2b)**, clustering into distinct dietary cohorts **(Fig. 2c)**. Trehalose feeding produced an exclusively upregulated lncRNA response, including *MSTRG.4316.8*, *MSTRG.2311.5,* and *XR_004782761.2* **(Fig. 2d)**, which resolved into a discrete expression signature **(Fig. 2e)**. Direct comparison between diets (glucose vs trehalose) demonstrated the high transcriptional divergence **(Fig. 2f)** and distinct response to nutritional states **(Fig. 2g)**, highlighted by upregulation of *MSTRG.13207.1* and *XR_004782677.2* alongside repression of *MSTRG.8126.1* and *MSTRG.13350.16*.

Cross-comparison overlap revealed that sugar responsiveness was largely treatment-specific: five differentially expressed lncRNAs (38%) were unique to glucose vs trehalose, four (31%) to glucose vs control, and three (23%) to trehalose vs control, with no lncRNA shared across all three groups **(Fig. S2a)**. Consistent with the RNAi dataset, sugar-responsive lncRNAs exhibited significantly lower baseline expression than protein-coding mRNAs (median normalized counts: 0.47 vs 1.26; Wilcoxon rank-sum test, $P < 2.2 \times 10^{-16}$; **Fig. S2b**). Furthermore, genomic feature profiling revealed a distribution broadly consistent with the RNAi dataset, dominated by intergenic (1,013), intronic (806), and antisense (450) lncRNAs, with an uneven genome-wide chromosomal distribution and a broad length profile predominantly concentrated around 1 kb **(Fig. 2h-j; Fig. S2c; Table S1)**. These results indicated that trehalose metabolism perturbation resulted in global changes in lncRNA expression dynamics, although structural characterizations are required to identify key lncRNAs involved in putative regulation.

Comparative structural analysis underpins trehalose metabolism perturbation responsive lncRNAs across different treatments

High-confidence differentially expressed lncRNAs, comprising 100 from the ds*SfTPS*–ds*SfTreh* RNAi and 14 from the sugar-fed transcriptome, were subjected to secondary-structure analysis to screen key deregulated and structurally stable lncRNAs. Based on normalized minimum free energy (MFE_norm ≤ −0.20 kcal/mol/nt) and ensemble diversity (Diversity_norm ≤ 0.20), 79 lncRNAs were classified as structurally stable, including 67 from the RNAi transcriptome and 12 from the sugar-fed transcriptome, whereas 35 were classified as structurally unstable **(Fig. 3a; Table S1)**.

Comparison of structurally stable differentially expressed lncRNAs across the six experimental contrasts revealed predominantly condition-specific distributions **(Fig. 3b)**. *MSTRG.4316.8* was shared between the glucose- and trehalose-fed conditions, *MSTRG.14909.1* between ds*SfTPS* vs control and ds*SfTPS* vs ds*SfTreh*, and *MSTRG.12532.1* and *MSTRG.13577.1* between ds*SfTreh* vs control and ds*SfTPS* vs ds*SfTreh*. *XR_007705431.1* was specific to the glucose-fed condition. At the transcriptome level, the RNAi dataset contained 65 unique structurally stable lncRNAs, whereas 10 were unique to the sugar-fed dataset, with only two genomic loci shared between the datasets **(Fig. 3c)**. *LOC118272830* was represented by *MSTRG.8126.1* in the sugar-fed dataset and *MSTRG.8083.1* in the RNAi dataset, whereas *LOC126912014* was represented by *MSTRG.9631.12* and *MSTRG.9545.3*, respectively. Classification of the combined 5,225 high-confidence lncRNAs showed comparable transcript composition between the two datasets **(Fig. 3d)**. XR-annotated lncRNAs constituted the largest category, with 1,588 and 1,586 transcripts in the RNAi and sugar-fed transcriptomes, respectively. Further followed by novel MSTRG transcripts (929 and 981) and a smaller proportion of reclassified putative lncRNAs (XM), comprising 72 and 69 transcripts, respectively.

Exon-number distributions were highly comparable between the two transcriptomes **(Fig. S3a)**. Two-exon lncRNAs represented the predominant class, comprising 1,285 RNAi and 1,334 sugar-fed transcripts, followed by three-exon (606 and 609), four-exon (303 and 289), five-exon (172 and 160), and ≥6-exon lncRNAs (223 and 244, respectively). Single-exon transcripts were absent following high-

confidence filtering, resulting in a predominance of lncRNAs containing two to three exons. Subcellular localization prediction further revealed a predominance of nuclear localization among structurally stable lncRNAs in both datasets, with smaller proportions assigned to the cytoplasm, ribosome, exosome, and cytosol **(Fig. S3b; Table S1)**.

Structurally stable lncRNAs also differed in predicted pseudoknot architecture between the two datasets. Sugar-fed lncRNAs exhibited a higher median pseudoknot count (63) than RNAi-associated lncRNAs (30) **(Fig. S3c; Table S1)**, together with a slightly higher median normalized pseudoknot density (0.035 vs 0.029) **(Fig. S3d; Table S1)**.

Candidate lncRNAs prioritized based on differential expression and structural stability, were examined across the sugar-fed and ds*SfTPS*–ds*SfTreh* RNAi transcriptomes through qRT-PCR for validation. In the sugar-fed transcriptome, *MSTRG.4316.8* and *MSTRG.9631.12* showed increased expression following glucose feeding, whereas *MSTRG.8126.1* exhibited high expression under trehalose feeding and *XR_007705431.1* showed reduced expression following glucose feeding **(Fig. 3e)**. qRT-PCR analysis supported these expression patterns, with *MSTRG.4316.8* **(Fig. 3f)** and *MSTRG.9631.12* **(Fig. 3g)** significantly induced following glucose feeding. Furthermore, *MSTRG.8126.1* was significantly induced following trehalose feeding **(Fig. 3h)**.

In the RNAi transcriptome, *MSTRG.8083.1* showed elevated expression following ds*SfTreh* silencing. While *MSTRG.9545.3*, *MSTRG.14909.1*, *MSTRG.12532.1*, and *MSTRG.13577.1* exhibited altered expression between the ds*SfTPS* and ds*SfTreh* treatments **(Fig. 3i)**. qRT-PCR analysis further supported the expression patterns of *MSTRG.12532.1* and *MSTRG.13577.1* **(Fig. 3j,k)**, both of which showed reduced expression following ds*SfTreh* silencing. The amplification of the selected candidate lncRNAs was further confirmed by agarose gel electrophoresis, which showed PCR products of the expected sizes, supporting the specificity of the qRT-PCR amplification **(Fig. S4a-c)**. Analyzed and selected key lncRNAs represent a putative group involved in trehalose metabolism gene regulation. In order to generate functional correlation obtaining coexpression profile and interaction network with target mRNA could be instrumental.

mRNA profiling uncovers discrete metabolic responses to genetic and dietary perturbations

Expression analysis of protein-coding transcripts revealed widespread, condition-specific reprogramming across all experimental cohorts, which could be used for further correlation with selected lncRNAs **(Fig. 4a-f; Fig. S5a-f; Table S2)**. Volcano plot and heatmap analyses demonstrated clear partitioning between treatment and control groups with robust biological reproducibility. Within the RNAi dataset, ds*SfTPS* vs control identified 141 differentially expressed genes (DEGs), whereas ds*SfTreh* vs control identified 540 DEGs **(Fig. 4a,b; Fig. S5a, b)**. The direct comparison between ds*SfTPS* vs ds*SfTreh* produced the largest transcriptional response, with 1152 DEGs **(Fig. 4c; Fig. S5c)** indicating markedly different downstream transcriptional responses following perturbation of trehalose synthesis and degradation. Under nutritional treatments, glucose and trehalose feeding resulted in 227 and 166 DEGs, respectively, relative to the control diet **(Fig. 4d,e; Fig. S5d, e)**, whereas the direct glucose vs trehalose comparison identified 140 DEGs **(Fig. 4f; Fig. S5f)**.

Cross-condition intersection and UpSet analyses confirmed that protein-coding responses were treatment-specific (**Fig. 4g–i**). In the RNAi model, the ds*SfTPS* vs ds*SfTreh* comparison encompassed the most number of unique DEGs (939), followed by ds*SfTreh* vs control (404) and ds*SfTPS* vs control (80) (**Fig. 4g**). Similarly, sugar-fed datasets showed limited transcriptomic overlap, with 155 unique DEGs in glucose vs control, 129 in trehalose vs control, and 83 in glucose vs trehalose (**Fig. 4h**). Integrated multi-contrast UpSet analysis established that the majority of DEGs remained restricted to individual experimental contrasts, underscoring specialized coding transcriptional programs responding to *SfTPS/SfTreh* suppression and dietary sugar shifts (**Fig. 4i**). Global mRNA expression analysis provided global profiling which could be further used for correlation with lncRNAs expression dynamics.

Co-expression network analysis reveals treatment-specific lncRNA-mRNA modules associated with trehalose metabolism

Co-expression network analysis of the ds*SfTPS* and ds*SfTreh* silencing transcriptomes revealed substantially larger, condition-specific lncRNA-mRNA networks **(Fig. 5a; Table S1)**. Following ds*SfTPS* silencing, *MSTRG.16172.1*, *MSTRG.12548.9*, *XR_007707652.1*, *MSTRG.14909.1*, and *MSTRG.8421.1* emerged

as hubs associated with multiple transcripts. In the ds*SfTPS* vs ds*SfTreh* comparison, *MSTRG.10987.5* was the predominant hub, exhibiting associations with 235 transcripts, followed by *MSTRG.12185.1*, *MSTRG.11284.1*, and *XR_007705962.1*. The most highly interconnected networks were observed following ds*SfTreh* silencing, where *XR_007707620.1*, *MSTRG.5468.3*, *XR_007706637.1*, *XR_004783195.2* and *MSTRG.10666.1* were associated with a significantly higher number of mRNAs.

The sugar-fed transcriptomes identified distinct hub lncRNAs that were extensively associated with protein-coding transcripts **(Fig. 5b; Table S1)**. In the glucose vs trehalose comparison, *MSTRG.13207.1* and *XM_035579964.2* emerged as the major hubs, exhibiting the highest numbers of associated mRNAs, followed by *MSTRG.13350.16*, *XR_004782677.2*, and *MSTRG.8126.1*. In the trehalose vs control comparison, *MSTRG.2311.5* and *MSTRG.4316.8* were the key hubs, followed by *XR_004782761.2* and *XR_007705604.1*. Several target mRNAs, including *LOC118265028*, *LOC118273804*, *LOC118268732*, *LOC118275125*, *LOC118278585*, and *LOC118267776*, were commonly shared among multiple hub lncRNAs, revealing interconnected co-expression modules associated with dietary sugar responses. Collectively, these networks identified distinct hub lncRNAs and extensive lncRNA-mRNA co-expression modules associated with nutritional and RNAi-mediated perturbation of trehalose metabolism.

Co-expression and RNA-RNA interaction analyses prioritize candidate lncRNA-*SfTRET1* regulatory modules

Gene Ontology (GO) analysis of mRNAs co-expressed with structurally stable DE lncRNAs revealed distinct functional profiles between the ds*SfTPS*-ds*SfTreh* RNAi and sugar-fed transcriptomes. In the RNAi transcriptome **(Fig. 5c)**, annotated biological processes were primarily associated with carbohydrate and energy metabolism, including glucose homeostasis, carbohydrate metabolic process, and transmembrane transport like facilitated trehalose transporter *SfTRET*. In contrast, the glucose- and trehalose-fed transcriptomes exhibited comparatively limited functional annotations **(Fig. 5d)**, with transmembrane transport, particularly *SfTRET*-mediated sugar transport, representing the annotated biological process. These results demonstrate that mRNAs co-expressed with structurally stable DE lncRNAs are putatively associated with carbohydrate transport and metabolism, and further identify

energy-associated processes following RNAi-mediated perturbation of trehalose metabolism.

Integration of co-expression, genomic localization, and RNA-RNA interaction analyses identified nine candidate lncRNA-mRNA pairs associated with trehalose transport. Genomic coordinate analysis showed that all candidate lncRNAs were located on chromosomes different from their respective *SfTRET1* loci. Seven lncRNAs associated with *LOC118277428*, *XR_007707652.1* with *LOC118270239*, and *XR_007705431.1* with *LOC126911554*, supporting their classification as putative trans-acting candidates (**Table S1)**. Predicted interaction sites were distributed across the 5′ UTR, CDS, and 3′ UTR of the corresponding *SfTRET1* transcripts **(Fig. S6)**. IntaRNA predicted favourable RNA-RNA interactions between lncRNAs and their targets, while RNAup and RNAcofold independently supported these interactions using accessibility and hybridization energies **(Table S1)**. Among these candidates, *MSTRG.6956.8–SfTRET1* exhibited the most favorable intaRNA interaction energy (ΔG = −23.79 kcal/mol), with additional support from RNAup (ΔG = −14.50 kcal/mol), and RNAcofold (ΔG = −15.21 kcal/mol). *XR_007707652.1* showed predicted interactions with three transcript isoforms of *LOC118270239*, whereas comparison of IntaRNA and RNAup prediction revealed overlapping or closely positioned interaction regions for *MSTRG.10987.5*, *MSTRG.11284.1*, *XR_007706201.1*, and *XR_007707652.1*. Together with their strong expression correlations (**|r|** = 0.95 to 0.97, $P < 0.005$) these independent computational analysis prioritized *MSTRG.4937.1* and *XR007706201.1–LOC118277428*, *XR_007707652.1–LOC118270239*, and *XR_007705431.1–LOC126911554* as candidate trans-associated regulatory modules for subsequent functional validation.

Expression analysis validates lncRNA-*SfTRET1* associations across trehalose metabolic perturbations

Co-expression analysis identified strong associations between several candidate lncRNAs and *SfTRET1* across dietary and RNAi-mediated perturbations of trehalose metabolism. Under sugar-fed conditions, *SfTRET1* (*LOC126911554*) exhibited a negative co-expression relationship with *XR_007705431.1* **(Fig. 6a)**. This inverse expression pattern was supported by qRT-PCR, which showed significant

upregulation of *SfTRET1* following glucose feeding, accompanied by significant downregulation of *XR_007705431.1* **(Fig. 6b, c)**. In the ds*SfTPS* treatment, both *SfTRET1* (*LOC118270239*) and *XR_007707652.1* were downregulated, consistent with the positive correlation observed in the transcriptomic analysis **(Fig. 6d–f)**. In the ds*SfTPS* vs ds*SfTreh* comparison, *SfTRET1* (*LOC118277428*) was positively correlated with *MSTRG.10987.5*, *MSTRG.11284.1*, *XR_007705962.1*, and *XR_007706201.1*, whereas *MSTRG.4937.1* and *MSTRG.6956.8* showed negative correlations with *SfTRET1* **(Fig. 6g)**. qRT-PCR analysis further examined the expression relationships between *SfTRET1* and selected candidate lncRNAs, including *XR_007706201.1*, *MSTRG.6956.8*, and *MSTRG.4937.1* **(Fig. 6h–k)**. Collectively, these results provide experimental support for the transcriptome-derived expression relationships between candidate lncRNAs and *SfTRET1* under dietary and RNAi-mediated perturbations of trehalose metabolism.

Silencing of *SfTRET1*-associated lncRNAs alters larval growth and *SfTRET1* expression

To investigate the functional roles of candidate *SfTRET1*-associated lncRNAs, *XR_007705431.1*, *XR_007706201.1*, and *MSTRG.4937.1* were individually silenced in *S. frugiperda* larvae by dsRNA-mediated RNAi **(Fig. S7a, b)**, and larval growth was monitored over six days **(Fig. 7a, b)**. Silencing of *XR_007705431.1* resulted in a progressive reduction in larval body weight relative to the dsGFP control **(Fig. 7a)**. Although no significant differences were detected at days 0 and 2, reduced body weight became apparent at day 4 ($P = 0.0733$) and was highly significant by day 6 ($P < 0.0001$). The growth-reducing phenotype was also evident from the smaller size of ds*XR_007705431.1*-treated larvae compared with dsGFP controls **(Fig. 7c)**. Consistent with the body-weight results, prolonged silencing of the candidate lncRNAs resulted in distinct developmental phenotypes, including differences in larval growth and progression to pupation compared with the dsGFP control **(Fig. S8a, b).**

qRT-PCR confirmed significant silencing of *XR_007705431.1* in dsRNA-treated larvae **(Fig. 7d)**. Notably, silencing of *XR_007705431.1* resulted in increased expression of *SfTRET1* (*LOC126911554*) relative to the dsGFP control **(Fig. 7e)**. This inverse expression response was consistent with the negative association

between *XR_007705431.1* and *SfTRET1* identified by co-expression analysis. In contrast, silencing of *XR_007706201.1* and *MSTRG.4937.1* resulted in increased larval body weight relative to the dsGFP control, particularly at the later stage of the feeding assay. No significant differences were observed at the earlier time points; however, by day 6, body weight was significantly increased following silencing of *MSTRG.4937.1* ($P = 0.0398$) and *XR_007706201.1* ($P < 0.0001$). The corresponding larval phenotypes were consistent with these growth responses **(Fig. 7f, i)**. qRT-PCR confirmed efficient silencing of *XR_007706201.1*, which was accompanied by decreased expression of *SfTRET1* (*LOC118277428*) (**Fig. 7g,h**). Conversely, silencing of *MSTRG.4937.1* resulted in increased *SfTRET1*(*LOC118277428*) expression (**Fig. 7j, k**). Collectively, functional silencing of the three candidate lncRNAs produced distinct effects on larval growth and *SfTRET1* expression, supporting their functional association with the regulation of trehalose transport and associated physiological responses.

Silencing of *SfTRET1*-associated lncRNAs is accompanied by distinct changes in trehalose and carbohydrate metabolism

To determine whether the growth and *SfTRET1* expression phenotypes associated with candidate lncRNA silencing were accompanied by metabolic changes, metabolite profiles were examined in larvae following silencing of *XR_007705431.1*, *XR_007706201.1*, and *MSTRG.4937.1* **(Fig. 8)**. Silencing of *XR_007705431.1*, which increased *SfTRET1* (*LOC126911554*) expression and reduced larval growth, produced a distinct metabolic profile relative to the dsGFP control **(Fig. 8a)**. Among the carbohydrate-associated metabolites, trehalose and glucose were significantly increased in ds*XR_007705431.1*-treated larvae (both $P = 0.0286$; **Fig. 8b, c)**. The broader metabolite profile also showed several amino acids and other key metabolites were also elevated, indicating that the metabolic response extended beyond trehalose-associated metabolites.

Silencing of the two lncRNAs associated with *SfTRET1* (*LOC118277428*) produced different metabolic responses **(Fig. 8d)**. Following *XR_007706201.1* silencing, which decreased *SfTRET1* expression and increased larval growth, trehalose showed a decreasing trend relative to dsGFP ($P = 0.0571$), whereas glucose showed a moderate increase that was not significant ($P =$

0.2000; **Fig. 8e, f)**. In contrast, silencing of *MSTRG.4937.1*, which increased *SfTRET1* (*LOC118277428*) expression and larval growth, was associated with increased trehalose (P = 0.0286; **Fig. 8g)** and a positive trend in glucose abundance (P = 0.0571; **Fig. 8h)**. Changes were also observed in several intermediates of central metabolism and amino acids, including increased fumarate, pyruvate, citrate, phenylalanine, cysteine, and methionine. Together with the corresponding larval growth phenotypes, these results associate lncRNA-dependent changes in *SfTRET1* expression with broader remodeling of trehalose and carbohydrate metabolic homeostasis in *S. frugiperda*.

Discussion

Systemic sugar homeostasis in insects requires precise coordination between trehalose synthesis, enzymatic hydrolysis, and facilitated transmembrane transport. Trehalose is synthesized predominantly in the fat body by TPS but utilized by multiple peripheral tissues through Treh-mediated hydrolysis. Its physiological availability at sink tissues depends on TRET1-family transporters function (Kikawada et al. 2007; Kanamori et al. 2010). Perturbation of any component of this TPS/TPP-trehalose-Treh/TRET axis can consequently alter carbohydrate homeostasis and produce broader metabolic and developmental effects. Despite the well-established importance of these metabolic components, the contribution of long lncRNAs to the regulation of trehalose homeostasis in insects remains enigmatic. Here, through integrative transcriptomics encompassing genetic knockdowns (ds*SfTPS* and ds*SfTreh*) and dietary sugar challenges, we identified and functionally characterized a robust repertoire of condition-responsive lncRNAs in *S. frugiperda*. Our findings identify candidate lncRNAs associated with *SfTRET1* expression and trehalose homeostasis, with functional silencing demonstrating their effects on *SfTRET1* expression, larval growth, and metabolic state.

The structural and thermodynamic properties of lncRNAs dictate their physiological stability and ribonucleoprotein interactomes. By integrating minimum free energy (MFE) thresholds with ensemble diversity filtering, we identified 79 structurally stable differentially expressed lncRNAs. Interestingly, sugar-responsive lncRNAs displayed a higher density of predicted pseudoknots compared to their RNAi-responsive counterparts. These higher-order structural motifs likely confer structural

resilience against ribonucleases in metabolically dynamic environments, facilitating sustained regulatory interactions (Peselis and Serganov 2014; Chillón and Marcia 2020). Furthermore, despite minimal transcript-level overlap between dietary and genetic perturbations, common genomic loci (*LOC118272830* and *LOC126912014*) responded across both conditions. This locus-level convergence highlights dedicated genomic hotspots that integrate nutritional cues and metabolic stress.

Trans-acting lncRNAs can interact with RNA, DNA, or RNA-binding proteins and thereby affect transcription, mRNA stability, processing and translation (Dykes and Emanueli 2017; Statello et al. 2021). Of particular relevance to the present findings, lncRNA-mRNA base pairing can either stabilize target transcripts and promote their expression or facilitate transcript degradation and translational repression, depending on the nature and location of the interaction (Yoon et al. 2013). Thus, the positive association between *XR_007707652.1* and *SfTRET1*, together with the negative association between XR_007705431.1 and SfTRET1, could arise through distinct post-transcriptional mechanisms. This possibility is strengthened by the preceding computational analyses, which classified these candidates as trans-associated because they reside on chromosomes different from their respective *SfTRET1* loci and predicted energetically favourable RNA-RNA interactions involving sites within the 5′ UTR, CDS, or 3′ UTR. RNA-RNA interactions are increasingly recognized as an important mechanism by which structured non-coding RNAs recognize and regulate RNA substrates, making the predicted complementarity between these lncRNAs and *SfTRET1* transcripts mechanistically plausible (Wang et al. 2022).

The involvement of these lncRNAs in carbohydrate regulation is also supported by the broader functional context of the co-expression networks. mRNAs associated with structurally stable DE lncRNAs were represented for glucose homeostasis, carbohydrate metabolism and transmembrane transport, while disruption of *SfTPS* and *SfTreh* additionally affected fatty-acid β-oxidation, fatty-acid biosynthesis and lipid catabolism. This metabolic connectivity is physiologically reasonable because insect carbohydrate and lipid reserves are tightly coordinated to meet changing energetic demands. In *S. frugiperda*, carbohydrate availability has long been associated with changes in trehalose, glycogen and energetic metabolism, and

more recent studies have further demonstrated extensive metabolic plasticity associated with feeding and energy-demanding physiological processes (Oliveira et al. 2022; Gokulanathan et al. 2024; Li et al. 2026). The observed lncRNA–*SfTRET1* relationships may therefore form part of a broader regulatory response that coordinates trehalose synthesis, hydrolysis, transport and alternative energy utilization rather than regulating an isolated transporter pathway.

A key finding of the present study was that functional perturbation of candidate lncRNAs produced distinct effects on *S. frugiperda* growth and *SfTRET1* expression. Silencing of *XR_007706201.1* and *MSTRG.4937.1* resulted in increased larval weight, suggesting that these lncRNAs may normally contribute, directly or indirectly, to regulatory processes that constrain growth. In contrast, silencing of *XR_007705431.1* significantly reduced larval weight while simultaneously increasing *SfTRET1* expression, providing a particularly strong functional connection between this lncRNA, trehalose transport, and larval development. *TRET1*-mediated transport is essential for the distribution of trehalose between tissues and maintenance of carbohydrate homeostasis, and perturbation of trehalose metabolism can markedly affect insect growth and development (Kanamori et al. 2010; Yang et al. 2024). Notably, the increase in *SfTRET1* following *XR_007705431.1* silencing is consistent with the negative association identified between these transcripts in the sugar-fed dataset and suggests that *XR_007705431.1* may negatively influence *SfTRET1* expression. However, the accompanying reduction in larval weight despite increased *SfTRET1* expression indicates that appropriate regulation of trehalose transport, rather than simply increased transporter abundance, may be required to maintain metabolic homeostasis and normal growth. Such bidirectional relationships are biologically plausible given the diverse mechanisms through which lncRNAs influence gene expression. The metabolomic responses further support a functional association between candidate lncRNAs, *SfTRET1* expression, and carbohydrate homeostasis. Silencing of *SflncXR_007705431.1* and *SflncMSTRG.4937.1*, both of which increased *SfTRET1* expression, was accompanied by increased trehalose abundance and a corresponding increase in glucose abundance, whereas *SflncXR_007706201.1* silencing reduced *SfTRET1* expression and showed a contrasting decrease in trehalose. This is biologically relevant because trehalose and glucose constitute closely interconnected components of insect carbohydrate

metabolism, and disruption of trehalose-metabolic genes in *S. frugiperda* alters the trehalose-glucose balance and produces growth and developmental abnormalities(Yang et al. 2024). The accompanying changes in glycolytic and TCA-cycle intermediates in our study further suggest that lncRNA perturbation is associated with broader metabolic remodelling rather than alteration of trehalose alone. Together with the corresponding growth phenotypes, these findings strengthen the association of the identified lncRNAs with the *SfTRET1*-linked metabolic network, although the steady-state metabolite measurements alone do not demonstrate changes in trehalose transport or metabolic flux.

Collectively, the present findings support a model in which nutritionally responsive and trehalose-metabolism-associated lncRNAs participate in regulatory networks linked to *SfTRET1* expression, providing a basis for subsequent functional characterization of lncRNA-mediated control of carbohydrate homeostasis in *S. frugiperda*.

Conclusion

In summary, this study provides an integrated view of lncRNA diversity, structural characteristics, expression dynamics, and functional associations with trehalose metabolism in *S. frugiperda*. We show that trehalose synthesis and hydrolysis perturbation, as well as dietary glucose and trehalose supplementation, elicits distinct lncRNA expression responses. We identified structurally stable and metabolically responsive lncRNAs associated with *SfTRET1* expression and predicted several potential trans-acting lncRNA-*SfTRET1* interactions. We found that silencing *Sflnc_XR007705431.1*, *Sflnc_XR007706201.1*, and *Sflnc_MSTRG.4937.1* altered *SfTRET1* expression, larval growth, and the relative abundance of trehalose, glucose, and other central metabolites, supporting their involvement in carbohydrate homeostasis. Together, our findings highlight lncRNAs as dynamic components of the insect metabolic regulatory network and provide experimentally supported candidates for future studies investigating their molecular interactions, transcript-level regulatory mechanisms, and potential relevance to insect growth and metabolic adaptation.

References

Altschul SF, Gish W, Miller W, Myers EW, Lipman DJ (1990) Basic local alignment search tool. Journal of Molecular Biology 215(3):403–410. https://doi.org/10.1016/S0022-2836(05)80360-2

Andrews et al. 2010 Andrews, S. (2010). FastQC: a quality control tool for high throughput sequence data. 2010.

Barbole RS, Sharma S, Patil Y, Giri AP, Joshi RS (2024) Chitinase inhibition induces transcriptional dysregulation altering ecdysteroid-mediated control of Spodoptera frugiperda development. iScience 27(3):109280. https://doi.org/10.1016/j.isci.2024.109280

Benjamini Y, Hochberg Y (1995) Controlling the False Discovery Rate: A Practical and Powerful Approach to Multiple Testing. Journal of the Royal Statistical Society Series B: Statistical Methodology 57(1):289–300. https://doi.org/10.1111/j.2517-6161.1995.tb02031.x

Bernhart SH, Tafer H, Mückstein U, Flamm C, Stadler PF, Hofacker IL (2006) Partition function and base pairing probabilities of RNA heterodimers. Algorithms Mol Biol 1(1):3. https://doi.org/10.1186/1748-7188-1-3

Buchfink B, Xie C, Huson DH (2015) Fast and sensitive protein alignment using DIAMOND. Nat Methods 12(1):59–60. https://doi.org/10.1038/nmeth.3176

Cao Z, Pan X, Yang Y, Huang Y, Shen H-B (2018) The lncLocator: a subcellular localization predictor for long non-coding RNAs based on a stacked ensemble classifier. Bioinformatics 34(13):2185–2194. https://doi.org/10.1093/bioinformatics/bty085

Chen H, Boutros PC (2011) VennDiagram: a package for the generation of highly-customizable Venn and Euler diagrams in R. BMC Bioinformatics 12(1):35. https://doi.org/10.1186/1471-2105-12-35

Chikate YR, Dawkar VV, Barbole RS, Tilak PV, Gupta VS, Giri AP (2016) Data of in vitro synthesized dsRNAs on growth and development of Helicoverpa armigera. Data in Brief 7:1602–1605. https://doi.org/10.1016/j.dib.2016.04.026

961 Chillón I, Marcia M (2020) The molecular structure of long non-coding RNAs: emerging
962 patterns and functional implications. Critical Reviews in Biochemistry and
963 Molecular Biology 55(6):662–690.
964 https://doi.org/10.1080/10409238.2020.1828259

965 Dykes IM, Emanueli C (2017) Transcriptional and Post-Transcriptional Gene
966 Regulation by Long Non-Coding RNA. Genomics, Proteomics & Bioinformatics
967 15(3):177–186. https://doi.org/10.1016/j.gpb.2016.12.005

968 Eddy SR (2011) Accelerated Profile HMM Searches. PLoS Comput Biol
969 7(10):e1002195. https://doi.org/10.1371/journal.pcbi.1002195

970 Fan X-N, Zhang S-W, Zhang S-Y, Ni J-J (2020) lncRNA_Mdeep: An Alignment-Free
971 Predictor for Distinguishing Long Non-Coding RNAs from Protein-Coding
972 Transcripts by Multimodal Deep Learning. IJMS 21(15):5222.
973 https://doi.org/10.3390/ijms21155222

974 Gokulanathan A, Mo H, Park Y (2024) Glucose influence cold tolerance in the fall
975 armyworm, Spodoptera frugiperda via trehalase gene expression. Sci Rep
976 14(1):27334. https://doi.org/10.1038/s41598-024-79082-y

977 Gotz S, Garcia-Gomez JM, Terol J, Williams TD, Nagaraj SH, Nueda MJ, Robles M,
978 Talon M, Dopazo J, Conesa A (2008) High-throughput functional annotation
979 and data mining with the Blast2GO suite. Nucleic Acids Research 36(10):3420–
980 3435. https://doi.org/10.1093/nar/gkn176

981 Gu Z, Eils R, Schlesner M (2016) Complex heatmaps reveal patterns and correlations
982 in multidimensional genomic data. Bioinformatics 32(18):2847–2849.
983 https://doi.org/10.1093/bioinformatics/btw313

984 Haas BJ, Papanicolaou A, Yassour M, Grabherr M, Blood PD, Bowden J, Couger MB,
985 Eccles D, Li B, Lieber M, MacManes MD, Ott M, Orvis J, Pochet N, Strozzi F,
986 Weeks N, Westerman R, William T, Dewey CN, Henschel R, LeDuc RD,
987 Friedman N, Regev A (2013) De novo transcript sequence reconstruction from
988 RNA-seq using the Trinity platform for reference generation and analysis. Nat
989 Protoc 8(8):1494–1512. https://doi.org/10.1038/nprot.2013.084

990 Huang Q, Zhang G, Nan J, Cheng W, Zhu-Salzman K (2021) Characterization of
991 trehalose metabolic genes and corresponding enzymatic activities during
992 diapause of Sitodiplosis mosellana. Journal of Insect Physiology 135:104324.
993 https://doi.org/10.1016/j.jinsphys.2021.104324

994 Jones P, Binns D, Chang H-Y, Fraser M, Li W, McAnulla C, McWilliam H, Maslen J,
995 Mitchell A, Nuka G, Pesseat S, Quinn AF, Sangrador-Vegas A, Scheremetjew
996 M, Yong S-Y, Lopez R, Hunter S (2014) InterProScan 5: genome-scale protein
997 function classification. Bioinformatics 30(9):1236–1240.
998 https://doi.org/10.1093/bioinformatics/btu031

999 Kalvari I, Nawrocki EP, Ontiveros-Palacios N, Argasinska J, Lamkiewicz K, Marz M,
1000 Griffiths-Jones S, Toffano-Nioche C, Gautheret D, Weinberg Z, Rivas E, Eddy
1001 SR, Finn RD, Bateman A, Petrov AI (2021) Rfam 14: expanded coverage of
1002 metagenomic, viral and microRNA families. Nucleic Acids Research
1003 49(D1):D192–D200. https://doi.org/10.1093/nar/gkaa1047

1004 Kanamori Y, Saito A, Hagiwara-Komoda Y, Tanaka D, Mitsumasu K, Kikuta S,
1005 Watanabe M, Cornette R, Kikawada T, Okuda T (2010) The trehalose
1006 transporter 1 gene sequence is conserved in insects and encodes proteins with
1007 different kinetic properties involved in trehalose import into peripheral tissues.
1008 Insect Biochemistry and Molecular Biology 40(1):30–37.
1009 https://doi.org/10.1016/j.ibmb.2009.12.006

1010 Kang Y-J, Yang D-C, Kong L, Hou M, Meng Y-Q, Wei L, Gao G (2017) CPC2: a fast
1011 and accurate coding potential calculator based on sequence intrinsic features.
1012 Nucleic Acids Research 45(W1):W12–W16. https://doi.org/10.1093/nar/gkx428

1013 Kikawada T, Saito A, Kanamori Y, Nakahara Y, Iwata K, Tanaka D, Watanabe M,
1014 Okuda T (2007) Trehalose transporter 1, a facilitated and high-capacity
1015 trehalose transporter, allows exogenous trehalose uptake into cells. Proc Natl
1016 Acad Sci USA 104(28):11585–11590.
1017 https://doi.org/10.1073/pnas.0702538104

Kim D, Paggi JM, Park C, Bennett C, Salzberg SL (2019) Graph-based genome alignment and genotyping with HISAT2 and HISAT-genotype. Nat Biotechnol 37(8):907–915. https://doi.org/10.1038/s41587-019-0201-4

Krueger F, James F, Ewels P, Afyounian E, Weinstein M, Schuster-Boeckler B, Hulselmans G, Sclamons (2023) FelixKrueger/TrimGalore: v0.6.10 - add default decompression path

Li M, Li M, Cai G, Dong Y, Guo Y, Shan Y, Li X, Jiang D, Liu P (2026) *Single-minded* regulates larval energy homeostasis in the fall armyworm *Spodoptera frugiperda*. Insect Science :1744-7917.70277. https://doi.org/10.1111/1744-7917.70277

Lorenz R, Bernhart SH, Höner Zu Siederdissen C, Tafer H, Flamm C, Stadler PF, Hofacker IL (2011) ViennaRNA Package 2.0. Algorithms Mol Biol 6(1):26. https://doi.org/10.1186/1748-7188-6-26

Love MI, Huber W, Anders S (2014) Moderated estimation of fold change and dispersion for RNA-seq data with DESeq2. Genome Biol 15(12):550. https://doi.org/10.1186/s13059-014-0550-8

Mann M, Wright PR, Backofen R (2017) IntaRNA 2.0: enhanced and customizable prediction of RNA–RNA interactions. Nucleic Acids Research 45(W1):W435–W439. https://doi.org/10.1093/nar/gkx279

Meng L-W, Luo Z-Y, Zhang F-Q, Dong Y-X, Ye C, Zhang W, Wang J-J (2025) Increased expression of an isoform of the long non-coding RNA, lnc37707, is associated with malathion resistance in Bactrocera dorsalis. Pesticide Biochemistry and Physiology 209:106343. https://doi.org/10.1016/j.pestbp.2025.106343

Mistry J, Chuguransky S, Williams L, Qureshi M, Salazar GA, Sonnhammer ELL, Tosatto SCE, Paladin L, Raj S, Richardson LJ, Finn RD, Bateman A (2021) Pfam: The protein families database in 2021. Nucleic Acids Research 49(D1):D412–D419. https://doi.org/10.1093/nar/gkaa913

1046 Mizuno H, Ueda K, Kobayashi Y, Tsuyama N, Todoroki K, Min JZ, Toyo'oka T (2017)
1047 The great importance of normalization of LC–MS data for highly-accurate non-
1048 targeted metabolomics. Biomedical Chromatography 31(1):e3864.
1049 https://doi.org/10.1002/bmc.3864

1050 Mohite S, Devkate T, Kalaskar P, Singh P, Subramanian A, Joshi RS (2026) Trehalose
1051 metabolism regulates transcriptional control of muscle development in
1052 lepidopteran insects

1053 Mückstein U, Tafer H, Hackermüller J, Bernhart SH, Stadler PF, Hofacker IL (2006)
1054 Thermodynamics of RNA–RNA binding. Bioinformatics 22(10):1177–1182.
1055 https://doi.org/10.1093/bioinformatics/btl024

1056 Muthu Lakshmi Bavithra C, Murugan M, Pavithran S, Naveena K (2023) Enthralling
1057 genetic regulatory mechanisms meddling insecticide resistance development
1058 in insects: role of transcriptional and post-transcriptional events. Front Mol
1059 Biosci 10:1257859. https://doi.org/10.3389/fmolb.2023.1257859

1060 Nawrocki EP, Eddy SR (2013) Infernal 1.1: 100-fold faster RNA homology searches.
1061 Bioinformatics 29(22):2933–2935. https://doi.org/10.1093/bioinformatics/btt509

1062 Oliveira NC, Phelan L, Labate CA, Cônsoli FL (2022) Non-targeted metabolomics
1063 reveals differences in the gut metabolic profile of the fall armyworm strains
1064 when feeding different food sources. Journal of Insect Physiology 139:104400.
1065 https://doi.org/10.1016/j.jinsphys.2022.104400

1066 Pertea G, Pertea M (2020) GFF Utilities: GffRead and GffCompare. F1000Res 9:304.
1067 https://doi.org/10.12688/f1000research.23297.2

1068 Pertea M, Kim D, Pertea GM, Leek JT, Salzberg SL (2016) Transcript-level expression
1069 analysis of RNA-seq experiments with HISAT, StringTie and Ballgown. Nat
1070 Protoc 11(9):1650–1667. https://doi.org/10.1038/nprot.2016.095

1071 Pertea M, Pertea GM, Antonescu CM, Chang T-C, Mendell JT, Salzberg SL (2015)
1072 StringTie enables improved reconstruction of a transcriptome from RNA-seq
1073 reads. Nat Biotechnol 33(3):290–295. https://doi.org/10.1038/nbt.3122

Peselis A, Serganov A (2014) Structure and function of pseudoknots involved in gene expression control. WIREs RNA 5(6):803–822. https://doi.org/10.1002/wrna.1247

Rahman M-M, Omoto C, Kim J (2024) Genome-Wide Exploration of Long Non-Coding RNAs of Helicoverpa armigera in Response to Pyrethroid Insecticide Resistance. Insects 15(3):146. https://doi.org/10.3390/insects15030146

Sato K, Kato Y (2022) Prediction of RNA secondary structure including pseudoknots for long sequences. Briefings in Bioinformatics 23(1):bbab395. https://doi.org/10.1093/bib/bbab395

Sato K, Kato Y, Hamada M, Akutsu T, Asai K (2011) IPknot: fast and accurate prediction of RNA secondary structures with pseudoknots using integer programming. Bioinformatics 27(13):i85–i93. https://doi.org/10.1093/bioinformatics/btr215

Satyavathi V, Ghosh R, Subramanian S (2017) Long Non-Coding RNAs Regulating Immunity in Insects. ncRNA 3(1):14. https://doi.org/10.3390/ncrna3010014

Shen W, Le S, Li Y, Hu F (2016) SeqKit: A Cross-Platform and Ultrafast Toolkit for FASTA/Q File Manipulation. PLoS ONE 11(10):e0163962. https://doi.org/10.1371/journal.pone.0163962

Shi J-F, Xu Q-Y, Guo W-C, Li G-Q (2016) Transcription changes of a putative trehalose-6-phosphate synthase gene in response to hormone stimulation in Leptinotarsa decemlineata (Say). Journal of Asia-Pacific Entomology 19(3):775–783. https://doi.org/10.1016/j.aspen.2016.07.003

Statello L, Guo C-J, Chen L-L, Huarte M (2021) Gene regulation by long non-coding RNAs and its biological functions. Nat Rev Mol Cell Biol 22(2):96–118. https://doi.org/10.1038/s41580-020-00315-9

Sun L, Luo H, Bu D, Zhao G, Yu K, Zhang C, Liu Y, Chen R, Zhao Y (2013) Utilizing sequence intrinsic composition to classify protein-coding and long non-coding transcripts. Nucleic Acids Research 41(17):e166–e166. https://doi.org/10.1093/nar/gkt646

Tang B, Wang S, Wang S-G, Wang H-J, Zhang J-Y, Cui S-Y (2018) Invertebrate Trehalose-6-Phosphate Synthase Gene: Genetic Architecture, Biochemistry, Physiological Function, and Potential Applications. Front Physiol 9:30. https://doi.org/10.3389/fphys.2018.00030

Tellis MB, Kotkar HM, Joshi RS (2023) Regulation of trehalose metabolism in insects: from genes to the metabolite window. Glycobiology 33(4):262–273. https://doi.org/10.1093/glycob/cwad011

Tsugawa H, Cajka T, Kind T, Ma Y, Higgins B, Ikeda K, Kanazawa M, VanderGheynst J, Fiehn O, Arita M (2015) MS-DIAL: data-independent MS/MS deconvolution for comprehensive metabolome analysis. Nat Methods 12(6):523–526. https://doi.org/10.1038/nmeth.3393

Wang D, Ye R, Cai Z, Xue Y (2022) Emerging roles of RNA – RNA interactions in transcriptional regulation. WIREs RNA 13(5):e1712. https://doi.org/10.1002/wrna.1712

Wang G, Gou Y, Guo S, Zhou J-J, Liu C (2021) RNA interference of trehalose-6-phosphate synthase and trehalase genes regulates chitin metabolism in two color morphs of Acyrthosiphon pisum Harris. Sci Rep 11(1):948. https://doi.org/10.1038/s41598-020-80277-2

Wickham H (2016) ggplot2. Springer International Publishing, Cham

Wu H, Sun C, Wu Y, Cao C, Sun L (2025) Physiological roles of trehalose in Hyphantria cunea revealed by RNA interference of trehalose-6-phosphate synthase and trehalase genes. Pesticide Biochemistry and Physiology 211:106422. https://doi.org/10.1016/j.pestbp.2025.106422

Xiao H, Ma C, Peng R, Xie M (2024) Insights into the role of non-coding RNAs in the development of insecticide resistance in insects. Front Genet 15:1429411. https://doi.org/10.3389/fgene.2024.1429411

Yang H-J, Cui M-Y, Zhao X-H, Zhang C-Y, Hu Y-S, Fan D (2023) Trehalose-6-phosphate synthase regulates chitin synthesis in Mythimna separata. Front Physiol 14:1109661. https://doi.org/10.3389/fphys.2023.1109661

Yang L, Wang Y, Lu Y, Li B, Chen K, Li C (2021) Genome-wide identification and characterization of long non-coding RNAs in *Tribolium castaneum*. Insect Science 28(5):1262–1276. https://doi.org/10.1111/1744-7917.12867

Yang Y, Liang Y, Zhi J, Li D, Li C (2024) Regulatory effect of trehalose metabolism on chitin synthesis in Spodoptera frugiperda (J. E. Smith) (Lepidoptera: Noctuidae) as determined using RNAi. Journal of Asia-Pacific Entomology 27(1):102179. https://doi.org/10.1016/j.aspen.2023.102179

Yoon J-H, Abdelmohsen K, Gorospe M (2013) Posttranscriptional Gene Regulation by Long Noncoding RNA. Journal of Molecular Biology 425(19):3723–3730. https://doi.org/10.1016/j.jmb.2012.11.024

Zhang H, Zhang L, Mathews DH, Huang L (2020) LinearPartition: linear-time approximation of RNA folding partition function and base-pairing probabilities. Bioinformatics 36(Supplement_1):i258–i267. https://doi.org/10.1093/bioinformatics/btaa460

Zheng X, Yuan J, Qian K, Tang Y, Wang J, Zhang Y, Feng J, Cao H, Xu B, Zhang Y, Liang P, Wu Q (2024) Identification and RNAi -based function analysis of trehalase family genes in *FRANKLINIELLA OCCIDENTALIS* (Pergande). Pest Management Science 80(6):2839–2850. https://doi.org/10.1002/ps.7992

Zhong F, Yu L, Jiang X, Chen Y, Wang S, Chao L, Jiang Z, He B, Xu C, Wang S, Tang B, Duan H, Wu Y (2023) Potential inhibitory effects of compounds ZK-PI-5 and ZK-PI-9 on trehalose and chitin metabolism in Spodoptera frugiperda (J. E. Smith). Front Physiol 14:1178996. https://doi.org/10.3389/fphys.2023.1178996

Zhou M, Shen Q, Wang S, Li G, Wu Y, Xu C, Tang B, Li C (2022) Regulatory function of the trehalose-6-phosphate synthase gene *TPS3* on chitin metabolism in brown planthopper, *Nilaparvata lugens*. Insect Molecular Biology 31(2):241–250. https://doi.org/10.1111/imb.12754

Zhu A, Ibrahim JG, Love MI (2019) Heavy-tailed prior distributions for sequence count data: removing the noise and preserving large differences. Bioinformatics 35(12):2084–2092. https://doi.org/10.1093/bioinformatics/bty895

Statements and Declarations

Funding

Vikram Nichit acknowledges the University Grants Commission, Government of India, for Junior Research Fellowship and Senior Research Fellowship support. This work was partially supported by projects GAP342926 and FIR020104.

Acknowledgements

The authors sincerely thank Anand Kumar Shukla for his valuable guidance in the *in silico* analyses. The authors are grateful to Dr. Suvasri Dutta for her critical review of the manuscript and constructive suggestions. The authors also thank Dr. Sharada Mohite, Bhagyashri Chaudhari, and Tanaji Devkate for their assistance in establishing the insect bioassays and generating the sugar-feeding and RNAi transcriptome datasets. The authors sincerely thank Tekchand Raut for his assistance with insect sample crushing.

Author contributions

V.N., and R.J. conceptualization; V.N., and R.J. methodology; V.N., and R.J. formal analysis; V.N., investigation; V.N., and R.J. visualization; V.N., *In-silco* data analysis; V.N.,R.J. writing – original draft; VB: Methodology, Reviewing and editing draft; R.J. writing – review and editing; R.J. resources; R.J. supervision, project administration, and funding acquisition.

Competing interests

The authors do not have any conflict of interest of any type.

Data availability

The RNA-seq datasets generated during this study have been deposited in the NCBI Sequence Read Archive (SRA). The sugar-feeding transcriptome dataset is available under BioProject accession PRJNA1497112 (https://dataview.ncbi.nlm.nih.gov/object/PRJNA1497112?reviewer=h9k25l1gtc2mc74r4pvegg1mgj), entitled "Comparative transcriptome analysis of *Spodoptera frugiperda* following trehalose and glucose Feeding." The RNA interference transcriptome dataset is available under BioProject accession PRJNA1497349

(https://dataview.ncbi.nlm.nih.gov/object/PRJNA1497349?reviewer=bfdo3su9teeg24j87ecvfspkd2), entitled *"*Transcriptome sequencing of *Spodoptera frugiperda* following ds*SfTPS* and ds*SfTreh* RNAi*."* Additional data supporting the findings of this study are provided within the article and its supplementary data files.

Figure legends:

Fig. 1 Genome-wide identification, differential expression, and genomic characterization of lncRNAs in the ds*SfTPS*–ds*SfTreh* RNAi transcriptome. **(a)** Workflow illustrating the identification and filtering of high-confidence lncRNAs from the ds*SfTPS*-ds*SfTreh* RNA-seq dataset. Raw sequencing reads were quality filtered and aligned to the reference genome followed by transcript assembly using StringTie. Multi-exonic transcripts (≥200 bp) were subjected to coding potential prediction using MDeep, CPC2, and CNCI. The intersecting candidate lncRNAs were further filtered by DIAMOND BLASTX searches against Swiss-Prot, Pfam, and Rfam analyses to remove protein-coding transcripts and housekeeping RNAs, yielding the final high-confidence lncRNA dataset. **(b)** Volcano plot showing differentially expressed lncRNAs between ds*SfTPS* and control. Red and blue dots represent significantly upregulated and downregulated lncRNAs, respectively, whereas grey dots indicate non-significant transcripts (adjusted $P \leq 0.05$ and $|\log2FC| > 1$). **(c)** Heatmap of significantly differentially expressed lncRNAs in ds*SfTPS* vs control generated using variance-stabilized transformed (VST) expression values. Expression values are shown as row-wise Z-scores with hierarchical clustering of genes and samples. **(d)** Volcano plot of differentially expressed lncRNAs in ds*SfTreh* vs control. Significantly upregulated and downregulated lncRNAs are highlighted in red and blue, respectively. **(e)** Heatmap of significantly differentially expressed lncRNAs in ds*SfTreh* vs control based on VST-normalized expression values and hierarchical clustering. **(f)** Volcano plot showing differential expression of lncRNAs between ds*SfTPS* vs ds*SfTreh* treatments. **(g)** Heatmap illustrating expression patterns of significantly differentially expressed lncRNAs between ds*SfTPS* vs ds*SfTreh*, with row-wise Z-score normalization and hierarchical clustering. **(h)** Genomic classification of the 2,589 high-confidence lncRNAs according to their relationship with protein-coding gene annotations, showing intergenic, intronic, antisense, splice-junction, same-strand exonic-overlap, exact-reference-match, and other categories. **(i)** Chromosomal distribution of the identified lncRNAs across the *S. frugiperda* genome; transcripts assigned to unplaced scaffolds were grouped as "Unplaced." **(j)** Distribution of individual lncRNA transcript lengths, shown as a violin plot with an embedded boxplot indicating the median and interquartile range.

Fig. 2 Identification and differential expression analysis of high-confidence lncRNAs in the sugar-fed transcriptome. (a) Workflow illustrating the identification and filtering of high-confidence lncRNAs from the sugar-fed RNA-seq dataset. Raw RNA-seq reads were quality filtered, aligned to the reference genome, and assembled using StringTie. Multi-exonic transcripts (≥200 bp) were subjected to coding potential prediction using MDeep, CPC2, and CNCI. The intersecting candidate lncRNAs were subsequently filtered by BLASTX, DIAMOND, Swiss-Prot, Pfam, and Rfam analyses to remove protein-coding transcripts and housekeeping RNAs, resulting in the final set of high-confidence lncRNAs. **(b)** Volcano plot showing differentially expressed lncRNAs between glucose-fed and control samples. Red and blue dots indicate significantly upregulated and downregulated lncRNAs, respectively, whereas grey dots represent non-significant transcripts (adjusted $P \leq 0.05$ and $|\log2FC| > 1$). **(c)** Heatmap of significantly differentially expressed lncRNAs in glucose-fed vs control generated using variance-stabilized transformed (VST) expression values. Expression values are displayed as row-wise Z-scores with hierarchical clustering of genes and samples. **(d)** Volcano plot showing differentially expressed lncRNAs between trehalose-fed and control samples. **(e)** Heatmap showing the expression profiles of significantly differentially expressed lncRNAs in trehalose-fed vs control, based on VST-normalized expression values and hierarchical clustering. **(f)** Volcano plot of differentially expressed lncRNAs between glucose-fed vs trehalose-fed treatments. **(g)** Heatmap illustrating the expression patterns of significantly differentially expressed lncRNAs between glucose-fed vs trehalose-fed samples using row-wise Z-score normalization and hierarchical clustering. **(h)** Genomic-location classification of the 2,636 high-confidence lncRNAs. **(i)** Chromosomal distribution of the identified lncRNAs across the *S. frugiperda* genome, with unplaced scaffolds grouped as “Unplaced.” **(j)** Distribution of individual lncRNA transcript lengths, shown as a violin plot with an embedded boxplot indicating the median and interquartile range.

Fig. 3 Structural characterization and expression validation of candidate lncRNAs across RNAi and sugar-fed transcriptomes (a) Structural stability landscape of high-confidence lncRNAs based on normalized minimum free energy (MFE/nt) and normalized ensemble diversity. Dashed lines indicate the thresholds used to classify structurally stable transcripts (MFE ≤ −0.20 kcal mol^{-1} nt^{-1} and

ensemble diversity ≤ 0.20 per nucleotide). Blue points represent structurally stable lncRNAs, whereas red points indicate structurally unstable lncRNAs. **(b)** UpSet plot showing the overlap of structurally stable lncRNAs identified among the differential expression comparisons from the two transcriptome datasets. Vertical bars indicate the number of lncRNAs within each intersection, whereas horizontal bars represent the total number of stable lncRNAs detected in each comparison. **(c)** Venn diagram illustrating the distribution of structurally stable lncRNAs between the glucose–trehalose sugar-fed transcriptome and the ds*SfTPS*–ds*SfTreh* RNAi transcriptome. A total of two stable lncRNAs were shared between the datasets, while ten and sixty-five stable lncRNAs were unique to the sugar-fed and RNAi transcriptomes, respectively. **(d)** Classification of high-confidence lncRNAs identified from the ds*SfTPS*-ds*SfTreh* RNAi and sugar-fed transcriptomes. Stacked bar plots show the numbers of annotated lncRNAs (XR), novel lncRNAs (MSTRG), and reclassified putative lncRNAs (XM) in each dataset. **(e)** Heatmap showing expression patterns of selected candidate lncRNAs across control (SFAD), glucose-fed (SFG), and trehalose-fed (SFT) samples. **(f-h)** qRT-PCR validation of selected lncRNAs under glucose- and trehalose-fed conditions. **(i)** Heatmap showing expression patterns of selected candidate lncRNAs across control (L4440), ds*SfTPS*, and ds*SfTreh* treatments. **(j,k)** qRT-PCR validation of selected lncRNAs following ds*SfTPS* and ds*SfTreh* treatments. Heatmap expression values are presented as row-wise Z-scores.

Fig. 4 Differential expression profiles of protein-coding transcripts across RNAi and sugar-fed transcriptomes. (a–c) Hierarchically clustered heatmaps of differentially expressed genes (DEGs) following ds*SfTPS* vs control, ds*SfTreh*vs control, and ds*SfTPS* vs ds*SfTreh*, respectively. **(d–f)** DEG expression profiles under glucose vs control, trehalose vs control, and glucose vs trehalose comparisons, respectively. Expression values are represented as row-wise Z-scores, with selected *SfTRET1* transcripts highlighted. **(g)** Venn diagram showing shared and comparison-specific DEGs among the three RNAi contrasts. **(h)** Venn diagram showing DEG overlap among the three sugar-fed comparisons. **(i)** UpSet plot summarizing shared and comparison-specific DEGs across the RNAi and sugar-fed transcriptomes.

Fig. 5 Co-expression network and Gene Ontology analysis of lncRNA-associated protein-coding genes in the ds*SfTPS*-ds*SfTreh* RNAi and sugar-fed transcriptomes. **(a)** Co-expression network of differentially expressed stable lncRNAs and their correlated protein-coding genes in the ds*SfTPS*-ds*SfTreh* RNAi transcriptome. Nodes represent lncRNAs and mRNAs, while edges indicate significant Pearson correlations ($|r| \geq 0.9$ threshold). Node colors denote transcript categories corresponding to the three pairwise comparisons (ds*SfTPS* vs control, ds*SfTreh* vs control, and ds*SfTPS* vs ds*SfTreh*), whereas edge colors indicate positive (green) and negative (red) correlations. Edge thickness is proportional to the absolute correlation coefficient, highlighting highly connected hub lncRNAs and mRNAs. **(b)** Co-expression network of differentially expressed stable lncRNAs and protein-coding genes in the sugar-fed transcriptome. Node colors distinguish lncRNAs identified from the glucose-fed vs control, trehalose-fed vs control, and glucose-fed vs trehalose-fed comparisons. Green and red edges represent positive and negative correlations, respectively, with edge width corresponding to the magnitude of the Pearson correlation coefficient. **(c)** Gene Ontology (GO) analysis of protein-coding genes co-expressed with lncRNAs in the ds*SfTPS*-ds*SfTreh* RNAi transcriptome. Annotated GO terms are grouped into the three major GO categories: Biological process (BP), Cellular component (CC), and Molecular function (MF). Horizontal bars indicate the number of upregulated (red) and downregulated (blue) genes associated with each annotated GO term. **(d)** Gene Ontology (GO) analysis of protein-coding genes co-expressed with lncRNAs in the sugar-fed transcriptome. Annotated GO terms are classified into Biological process, Cellular component, and Molecular function, with horizontal bar plots representing the numbers of upregulated (red) and downregulated (blue) genes assigned to each functional category. These analyses highlight the biological processes and molecular functions potentially regulated by the identified lncRNA–mRNA co-expression modules.

Fig. 6 Co-expression and qRT-PCR validation of candidate lncRNA–*SfTRET1* expression relationships. (a) Co-expression heatmap showing the negative association between *SfTRET1* (LOC126911554) and XR_007705431.1 under glucose-fed conditions. **(b, c)** qRT-PCR validation of *SfTRET1* (LOC126911554) and XR_007705431.1 expression, respectively, following glucose feeding. **(d)** Co-expression heatmap showing the positive association between *SfTRET1*(LOC118270239) and XR_007707652.1 following ds*SfTPS* treatment. **(e, f)** qRT-PCR validation of *SfTRET1*(LOC118270239) and XR_007707652.1 expression, respectively, following ds*SfTPS* treatment. **(g)** Co-expression profiles of *SfTRET1* (LOC118277428) with positively and negatively correlated candidate lncRNAs in the ds*SfTPS* vs ds*SfTreh* comparison. **(h–k)** qRT-PCR validation of *SfTRET1* (LOC118277428), *XR_007706201.1*, *MSTRG.6956.8*, and *MSTRG.4937.1*, respectively. Heatmap values represent row-wise standardized expression (Z-scores), and correlation coefficients (*r*) are indicated for the corresponding lncRNA–*SfTRET1* relationships.

Fig. 7 Functional silencing of candidate lncRNAs alters *SfTRET1* expression and larval growth in *S. frugiperda*. (a) Temporal changes in larval body weight following silencing of *lnc_XR_007705431.1* compared with the dsGFP control. **(b)** Temporal changes in larval body weight following silencing of *Sflnc_XR_007706201.1* and *Sflnc_MSTRG.4937.1* compared with dsGFP-treated larvae. **(c)** Representative larval phenotypes following *Sflnc_XR_007705431.1* silencing compared with the dsGFP control. **(d)** qRT-PCR validation of *Sflnc_XR_007705431.1* silencing efficiency. **(e)** Relative expression of *SfTRET1* (*LOC126911554*) following *Sflnc_XR_007705431.1* silencing. **(f)** Representative larval phenotypes following *Sflnc_XR_007706201.1* silencing compared with dsGFP-treated larvae. **(g)** qRT-PCR validation of *Sflnc_XR_007706201.1* silencing efficiency. **(h)** Relative expression of *SfTRET1* (*LOC118277428*) following *Sflnc_XR_007706201.1* silencing. **(i)** Representative larval phenotypes following *lnc_MSTRG.4937.1* silencing compared with the dsGFP control. **(j)** qRT-PCR validation of *Sflnc_MSTRG.4937.1* silencing efficiency. **(k)** Relative expression of *SfTRET1* (*LOC118277428*) following *Sflnc_MSTRG.4937.1* silencing. Bars

represent mean ± SEM, and the corresponding *P*-values are indicated above comparisons.

Fig. 8 Metabolic changes associated with silencing of *SfTRET1*-associated lncRNAs in *Spodoptera frugiperda*. (a) Heatmap showing relative metabolite abundance following silencing of *SflncXR_007705431.1* compared with the dsGFP control. **(b, c)** Trehalose and glucose abundance, respectively, in dsGFP- and ds*SflncXR_007705431.1*-treated larvae. **(d)** Heatmap showing relative metabolite abundance following silencing of *SflncXR_007706201.1* and *SflncMSTRG.4937.1* compared with the dsGFP control. **(e, f)** Trehalose and glucose abundance, respectively, following ds*SflncXR_007706201.1* silencing. **(g, h)** Trehalose and glucose abundance, respectively, following ds*SflncMSTRG.4937.1* silencing. For heatmaps, metabolite abundances were log2-transformed and standardized by row-wise Z-score; red and blue indicate relatively higher and lower abundance, respectively. Hierarchical clustering was performed for metabolites and independently among biological replicates within each treatment group. Values adjacent to the heatmaps indicate log2 fold change (log2FC) relative to dsGFP and corresponding *P* values. Bar plots show mean ± SEM, with individual treatments compared with dsGFP using two-sided Mann–Whitney U tests. *P* values are indicated above the comparisons.

Supplementary figure legends:

Fig. S1 Differential expression overlap and transcript-length characteristics of lncRNAs in the ds*SfTPS*–ds*SfTreh* RNAi transcriptome. (a) Venn diagram showing shared and comparison-specific differentially expressed lncRNAs among ds*SfTPS* vs control, ds*SfTreh* vs control, and ds*SfTPS* vs ds*SfTreh*. **(b)** Comparison of normalized expression levels between the identified lncRNAs and protein-coding mRNAs; sample sizes, median values, and statistical significance are indicated. **(c)** Length distribution of the 2,589 high-confidence lncRNAs across four transcript-size classes.

Fig. S2 Differential expression overlap and transcript-length characteristics of lncRNAs in the sugar-fed transcriptome. (a) Venn diagram showing shared and comparison-specific differentially expressed lncRNAs among glucose vs control, trehalose vs control, and glucose vs trehalose comparisons. **(b)** Comparison of normalized expression levels between lncRNAs and protein-coding mRNAs; sample sizes, median values, and statistical significance are indicated. **(c)** Length distribution of the 2,636 high-confidence lncRNAs across four transcript-size classes.

Fig. S3 Structural features and predicted subcellular localization of lncRNAs identified from the RNAi and sugar-fed transcriptomes. (a) Exon-number distribution of high-confidence lncRNAs in the ds*SfTPS*–ds*SfTreh* RNAi and sugar-fed datasets. **(b)** Predicted subcellular localization of lncRNAs across the nucleus, cytoplasm, cytosol, exosome, and ribosome. **(c, d)** Comparison of predicted pseudoknot counts and pseudoknot density, respectively, among structurally stable lncRNAs from the sugar-fed and RNAi transcriptomes; median values are indicated.

Fig. S4 Agarose gel validation of candidate lncRNA amplification upon quantitative real-time PCR analysis. (a) Agarose gel electrophoresis showing RT-PCR amplification of candidate lncRNAs *MSTRG.4316.8* and *MSTRG.9631.12* under artificial diet (AD control), glucose-fed, and trehalose-fed conditions. Amplification products were resolved on agarose gels alongside a DNA size marker, with the expected amplicon size of approximately 500 bp indicated. **(b)** Agarose gel validation of *XR_007705431.1* and *MSTRG.8126.1* amplified from glucose-fed and trehalose-fed samples. Distinct single PCR products of the expected size confirmed successful

amplification before downstream qRT-PCR analysis. **(c)** Agarose gel validation of *MSTRG.8083.1*, *MSTRG.12532.1*, and *MSTRG.13577.1* amplified from L4440 control and ds*SfTreh* RNAi samples. Representative PCR products of the expected size (~500 bp) demonstrate the specificity of primer amplification used for subsequent quantitative expression analyses. DNA ladders were included as molecular size markers in each gel.

Fig. S5 Differential expression profiles of protein-coding transcripts across RNAi and sugar-fed conditions. Volcano plots showing differentially expressed mRNAs in **(a)** ds*SfTPS* vs control, **(b)** ds*SfTreh* vs control, **(c)** ds*SfTPS*vs ds*SfTreh*, **(d)** glucose vs control, **(e)** trehalose vs control, and **(f)** glucose vs trehalose comparisons. Red and blue points represent significantly upregulated and downregulated transcripts, respectively, while grey points indicate non-significant transcripts. Dashed lines indicate the applied fold-change and adjusted *P*-value thresholds; selected highly significant transcripts are labelled.

Fig. S6 Predicted interaction sites of candidate lncRNAs on the *SfTRET1* transcript (XM_035596214.2). Schematic representation of the predicted binding positions of seven candidate lncRNAs on the *SfTRET1* (*XM_035596214.2*) transcript based on IntaRNA interaction analysis. The transcript is divided into the 5′ untranslated region (5′ UTR; nucleotides 1–277), coding sequence (CDS; nucleotides 278–1741), and 3′ untranslated region (3′ UTR; nucleotides 1742–2139). Colored horizontal bars indicate the predicted binding regions of individual lncRNAs, with blue representing positively correlated lncRNAs and red representing negatively correlated lncRNAs based on Pearson correlation analysis.

Fig. S7 Confirmation of dsRNA production for candidate *Spodoptera frugiperda* lncRNAs by agarose gel electrophoresis. (a) Agarose gel showing dsRNA production in IPTG-induced and uninduced *E. coli* HT115 cultures carrying L4440 constructs for the dsGFP control and *lnc_XR_007705431.1*. **(b)** Agarose gel showing dsRNA production in induced and uninduced cultures carrying L4440 constructs for *lnc_XR_007706201.1* and *lnc_MSTRG.4937.1*. Distinct bands corresponding to the expected dsRNA products were detected predominantly in the induced cultures, confirming IPTG-dependent dsRNA production. Molecular size

markers are shown on the left, with the 500-bp position indicated. Red boxes highlight the corresponding dsRNA bands.

Fig. S8 Developmental phenotypes of *Spodoptera frugiperda* following prolonged silencing of candidate *SfTRET1*-associated lncRNAs. Representative larval and pupal phenotypes recorded on day 10 following dsRNA-mediated silencing of candidate lncRNAs. **(a)** Developmental phenotypes of ds*SfXR_007705431.1*-treated insects compared with the dsGFP control, showing delayed developmental progression and a higher proportion of larvae remaining at the larval stage in the silenced group. **(b)** Representative phenotypes following silencing of *SfXR_007706201.1* and *SfMSTRG.4937.1* compared with the dsGFP control. Images show the developmental stages present in each treatment at day 10; scale is shown in centimeters.

Supplementary Information:

Table S1. Identification and characterization of lncRNAs from the ds*SfTPS*- and ds*SfTreh*-silenced transcriptomes and the sugar-fed transcriptome.

Table S2. Differentially expressed genes (DEGs) identified from the ds*SfTPS*- and ds*SfTreh*-silenced transcriptomes and the sugar-fed transcriptome.

Table S3. Primers used in this study.

Figure 1

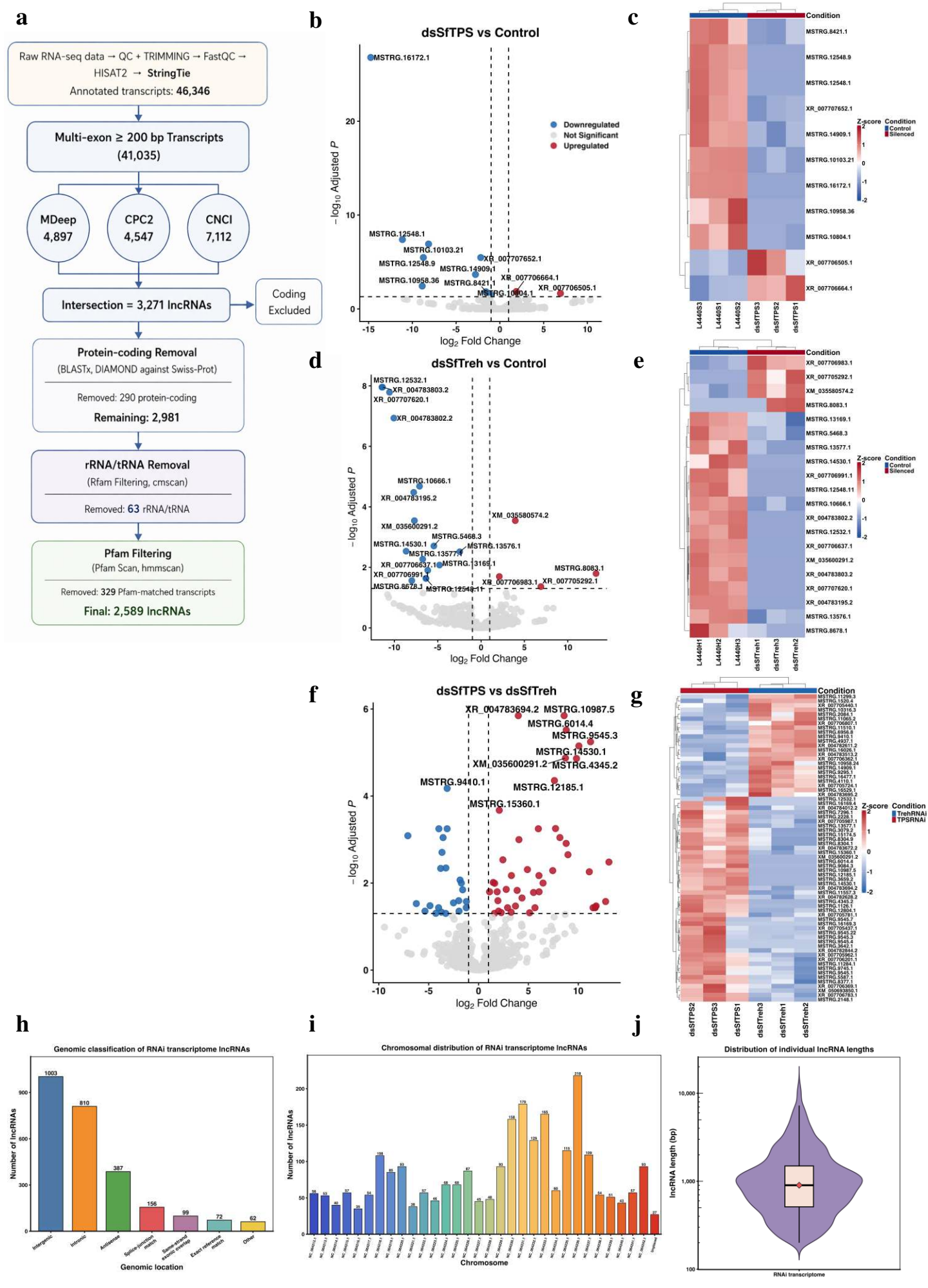

a
Raw RNA-seq data → QC + TRIMMING → FastQC → HISAT2 → StringTie
Annotated transcripts: 46,346
Multi-exon ≥ 200 bp Transcripts (41,035)
MDeep 4,897
CPC2 4,547
CNCI 7,112
Intersection = 3,271 lncRNAs
Coding Excluded
Protein-coding Removal
(BLASTx, DIAMOND against Swiss-Prot)
Removed: 290 protein-coding
Remaining: 2,981
rRNA/tRNA Removal
(Rfam Filtering, cmscan)
Removed: 63 rRNA/tRNA
Pfam Filtering
(Pfam Scan, hmmscan)
Removed: 329 Pfam-matched transcripts
Final: 2,589 lncRNAs
b
dsSfTPS vs Control
Downregulated
Not Significant
Upregulated
−log10 Adjusted P
log2 Fold Change
c
Condition
Control
Silenced
Z-score
L4440S3
L4440S1
L4440S2
dsSfTPS3
dsSfTPS2
dsSfTPS1
d
dsSfTreh vs Control
e
TrehRNAi
TPSRNAi
dsSfTreh1
dsSfTreh3
dsSfTreh2
L4440H1
L4440H2
L4440H3
f
dsSfTPS vs dsSfTreh
g
h
Genomic classification of RNAi transcriptome lncRNAs
Number of lncRNAs
Genomic location
Intergenic
Intronic
Antisense
Splice-junction match
Same-strand exonic overlap
Exact reference match
Other
i
Chromosomal distribution of RNAi transcriptome lncRNAs
Chromosome
j
Distribution of individual lncRNA lengths
lncRNA length (bp)
RNAi transcriptome

Figure 2

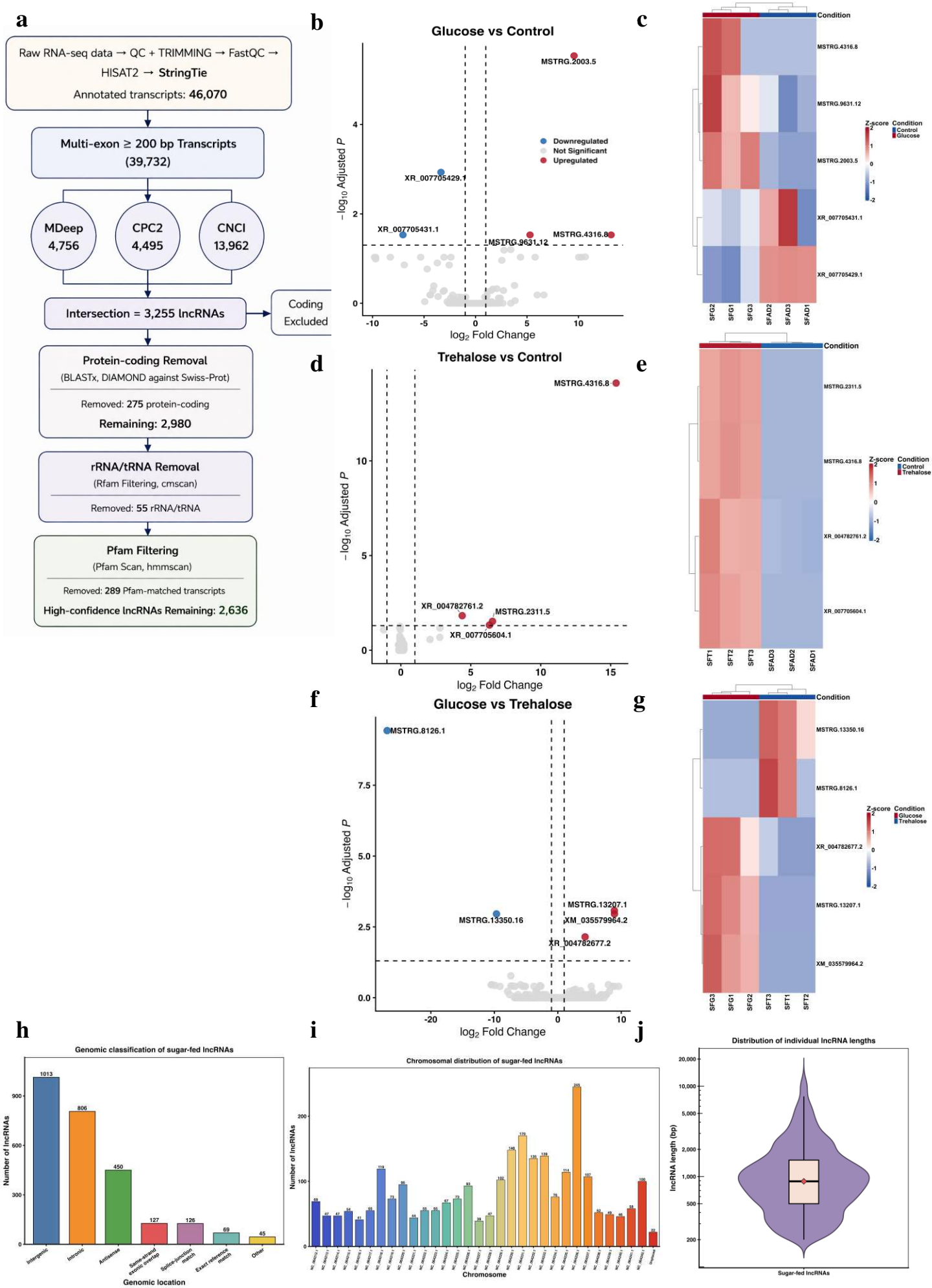

a
Raw RNA-seq data → QC + TRIMMING → FastQC → HISAT2 → StringTie
Annotated transcripts: 46,070
Multi-exon ≥ 200 bp Transcripts (39,732)
MDeep 4,756
CPC2 4,495
CNCI 13,962
Intersection = 3,255 lncRNAs
Coding Excluded
Protein-coding Removal
(BLASTx, DIAMOND against Swiss-Prot)
Removed: 275 protein-coding
Remaining: 2,980
rRNA/tRNA Removal
(Rfam Filtering, cmscan)
Removed: 55 rRNA/tRNA
Pfam Filtering
(Pfam Scan, hmmscan)
Removed: 289 Pfam-matched transcripts
High-confidence lncRNAs Remaining: 2,636
b
Glucose vs Control
MSTRG.2003.5
Downregulated
Not Significant
Upregulated
XR_007705429.1
XR_007705431.1
MSTRG.9631.12
MSTRG.4316.8
−log10 Adjusted P
log2 Fold Change
c
Condition
Control
Glucose
Z-score
MSTRG.4316.8
MSTRG.9631.12
MSTRG.2003.5
XR_007705431.1
XR_007705429.1
SFG2
SFG1
SFG3
SFAD2
SFAD3
SFAD1
d
Trehalose vs Control
MSTRG.4316.8
XR_004782761.2
MSTRG.2311.5
XR_007705604.1
e
Condition
Control
Trehalose
MSTRG.2311.5
MSTRG.4316.8
XR_004782761.2
XR_007705604.1
SFT1
SFT2
SFT3
SFAD3
SFAD2
SFAD1
f
Glucose vs Trehalose
MSTRG.8126.1
MSTRG.13350.16
MSTRG.13207.1
XM_035579964.2
XR_004782677.2
g
Condition
Glucose
Trehalose
MSTRG.13350.16
MSTRG.8126.1
XR_004782677.2
MSTRG.13207.1
XM_035579964.2
SFG3
SFG1
SFG2
SFT3
SFT1
SFT2
h
Genomic classification of sugar-fed lncRNAs
Number of lncRNAs
1013
806
450
127
126
69
45
Intergenic
Intronic
Antisense
Same-strand exonic overlap
Splice-junction match
Exact reference match
Other
Genomic location
i
Chromosomal distribution of sugar-fed lncRNAs
Number of lncRNAs
Chromosome
j
Distribution of individual lncRNA lengths
lncRNA length (bp)
Sugar-fed lncRNAs

Figure 3

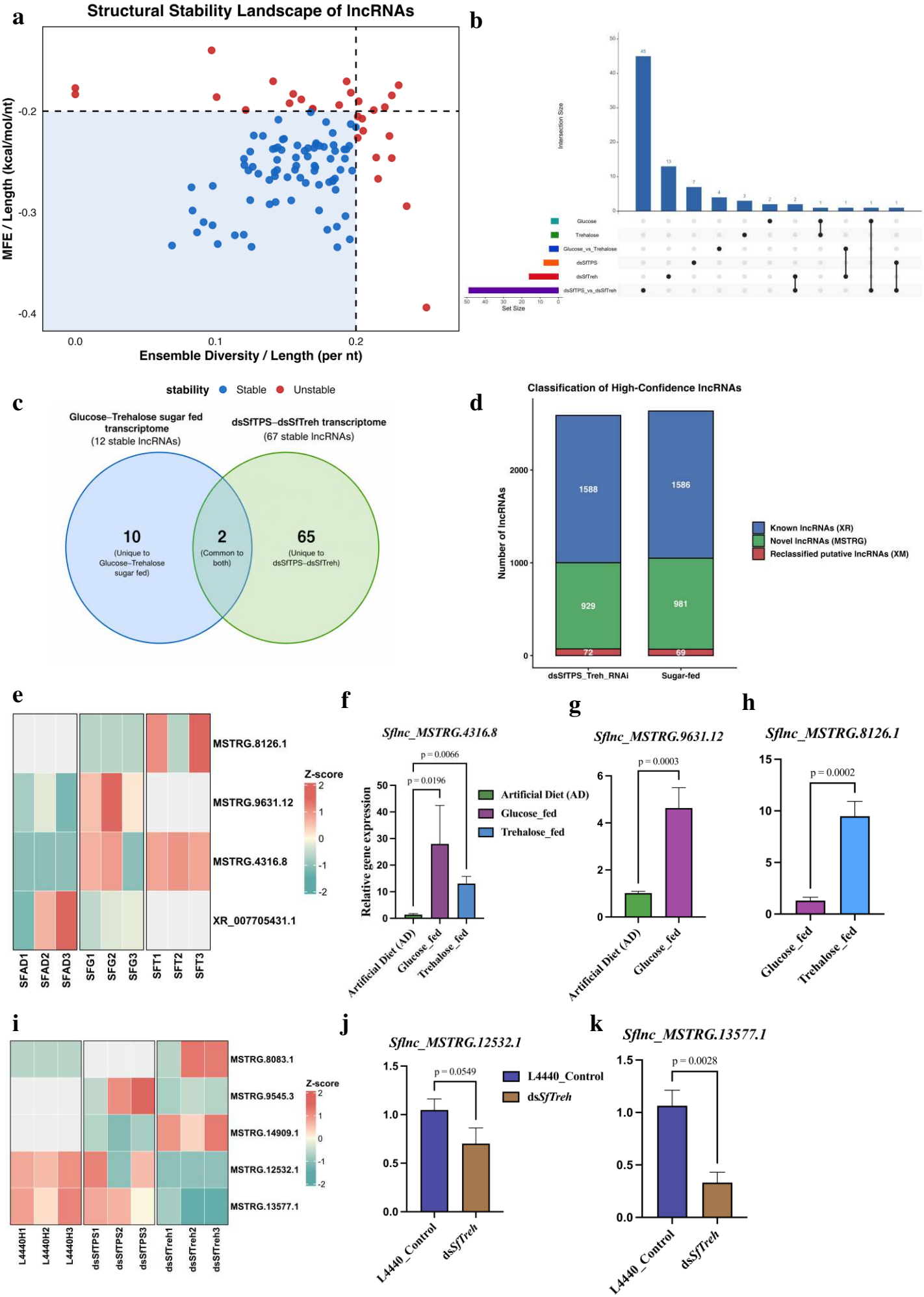

a
Structural Stability Landscape of lncRNAs
MFE / Length (kcal/mol/nt)
Ensemble Diversity / Length (per nt)
b
Intersection Size
Set Size
Glucose
Trehalose
Glucose_vs_Trehalose
dsSfTPS
dsSfTreh
dsSfTPS_vs_dsSfTreh
c
stability Stable Unstable
Glucose–Trehalose sugar fed transcriptome
(12 stable lncRNAs)
dsSfTPS–dsSfTreh transcriptome
(67 stable lncRNAs)
10
(Unique to Glucose–Trehalose sugar fed)
2
(Common to both)
65
(Unique to dsSfTPS–dsSfTreh)
d
Classification of High-Confidence lncRNAs
Number of lncRNAs
1588
1586
929
981
72
69
dsSfTPS_Treh_RNAi
Sugar-fed
Known lncRNAs (XR)
Novel lncRNAs (MSTRG)
Reclassified putative lncRNAs (XM)
e
MSTRG.8126.1
MSTRG.9631.12
MSTRG.4316.8
XR_007705431.1
Z-score
SFAD1 SFAD2 SFAD3 SFG1 SFG2 SFG3 SFT1 SFT2 SFT3
f
Sflnc_MSTRG.4316.8
p = 0.0066
p = 0.0196
Relative gene expression
Artificial Diet (AD)
Glucose_fed
Trehalose_fed
g
Sflnc_MSTRG.9631.12
p = 0.0003
h
Sflnc_MSTRG.8126.1
p = 0.0002
i
MSTRG.8083.1
MSTRG.9545.3
MSTRG.14909.1
MSTRG.12532.1
MSTRG.13577.1
Z-score
L4440H1 L4440H2 L4440H3 dsSfTPS1 dsSfTPS2 dsSfTPS3 dsSfTreh1 dsSfTreh2 dsSfTreh3
j
Sflnc_MSTRG.12532.1
p = 0.0549
L4440_Control
dsSfTreh
k
Sflnc_MSTRG.13577.1
p = 0.0028

Figure 4

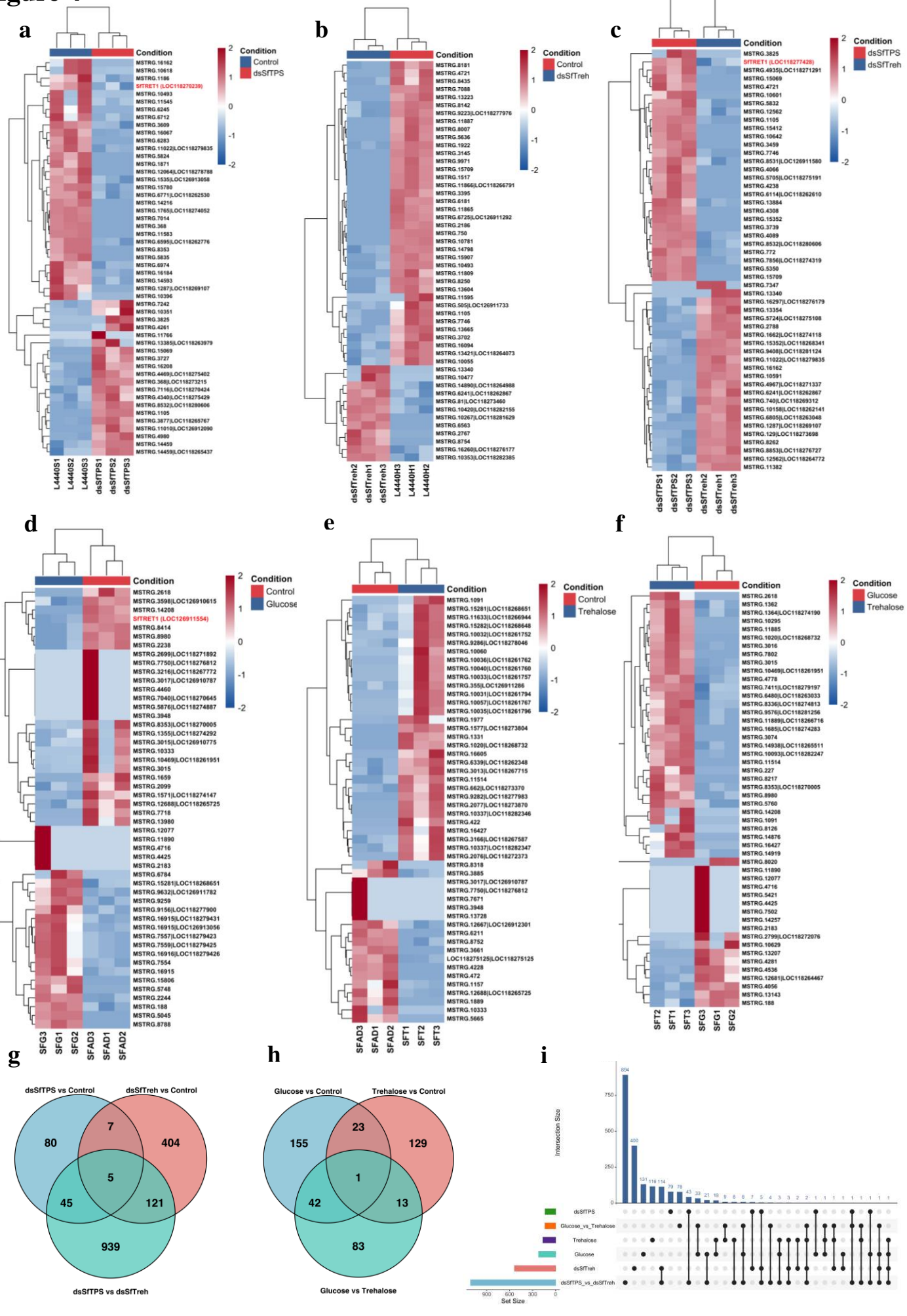

a
Condition
Control
dsSfTPS
SfTRET1 (LOC118270239)
L4440S1
L4440S2
L4440S3
dsSfTPS1
dsSfTPS2
dsSfTPS3
b
Condition
Control
dsSfTreh
dsSfTreh2
dsSfTreh1
dsSfTreh3
L4440H3
L4440H1
L4440H2
c
Condition
dsSfTPS
dsSfTreh
SfTRET1 (LOC118277428)
dsSfTPS1
dsSfTPS2
dsSfTPS3
dsSfTreh2
dsSfTreh1
dsSfTreh3
d
Condition
Control
Glucose
SfTRET1 (LOC126911554)
SFG3
SFG1
SFG2
SFAD3
SFAD1
SFAD2
e
Condition
Control
Trehalose
SFAD3
SFAD1
SFAD2
SFT1
SFT2
SFT3
f
Condition
Glucose
Trehalose
SFT2
SFT1
SFT3
SFG3
SFG1
SFG2
g
dsSfTPS vs Control
dsSfTreh vs Control
dsSfTPS vs dsSfTreh
80
7
404
5
45
121
939
h
Glucose vs Control
Trehalose vs Control
Glucose vs Trehalose
155
23
129
1
42
13
83
i
Intersection Size
Set Size
dsSfTPS
Glucose_vs_Trehalose
Trehalose
Glucose
dsSfTreh
dsSfTPS_vs_dsSfTreh

Figure 5

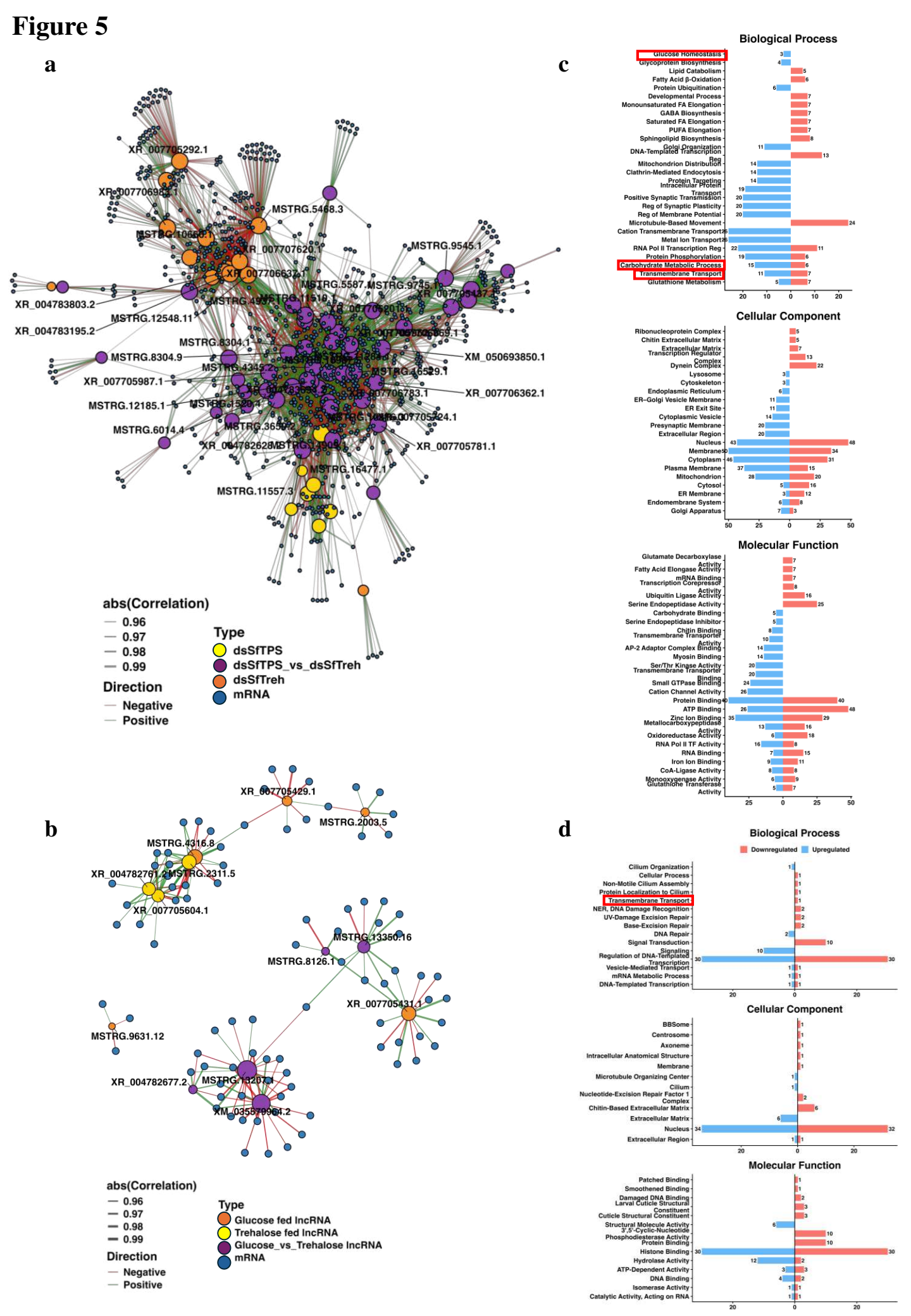

a
XR_007705292.1
MSTRG.5468.3
MSTRG.9545.1
XR_007707620.1
XR_004783803.2
MSTRG.12548.11
XR_004783195.2
MSTRG.8304.1
MSTRG.8304.9
XM_050693850.1
XR_007705987.1
XR_007706362.1
MSTRG.12185.1
MSTRG.6014.4
XR_007705781.1
MSTRG.16477.1
MSTRG.11557.3
abs(Correlation)
0.96
0.97
0.98
0.99
Direction
Negative
Positive
Type
dsSfTPS
dsSfTPS_vs_dsSfTreh
dsSfTreh
mRNA
b
XR_007705429.1
MSTRG.2003.5
MSTRG.4316.8
XR_004782761.2
MSTRG.2311.5
XR_007705604.1
MSTRG.13350.16
MSTRG.8126.1
XR_007705431.1
MSTRG.9631.12
XR_004782677.2
XM_035679964.2
abs(Correlation)
0.96
0.97
0.98
0.99
Direction
Negative
Positive
Type
Glucose fed lncRNA
Trehalose fed lncRNA
Glucose_vs_Trehalose lncRNA
mRNA
c
Biological Process
Glucose Homeostasis
Glycoprotein Biosynthesis
Lipid Catabolism
Fatty Acid β-Oxidation
Protein Ubiquitination
Developmental Process
Monounsaturated FA Elongation
GABA Biosynthesis
Saturated FA Elongation
PUFA Elongation
Sphingolipid Biosynthesis
Golgi Organization
DNA-Templated Transcription
Rho
Mitochondrion Distribution
Clathrin-Mediated Endocytosis
Protein Targeting
Intracellular Protein Transport
Positive Synaptic Transmission
Reg of Synaptic Plasticity
Reg of Membrane Potential
Microtubule-Based Movement
Cation Transmembrane Transport
Metal Ion Transport
RNA Pol II Transcription Reg
Protein Phosphorylation
Carbohydrate Metabolic Process
Transmembrane Transport
Glutathione Metabolism
Cellular Component
Ribonucleoprotein Complex
Chitin Extracellular Matrix
Extracellular Matrix
Transcription Regulator Complex
Dynein Complex
Lysosome
Cytoskeleton
Endoplasmic Reticulum
ER–Golgi Vesicle Membrane
ER Exit Site
Cytoplasmic Vesicle
Presynaptic Membrane
Extracellular Region
Nucleus
Membrane
Cytoplasm
Plasma Membrane
Mitochondrion
Cytosol
ER Membrane
Endomembrane System
Golgi Apparatus
Molecular Function
Glutamate Decarboxylase Activity
Fatty Acid Elongase Activity
mRNA Binding
Transcription Corepressor Activity
Ubiquitin Ligase Activity
Serine Endopeptidase Activity
Carbohydrate Binding
Serine Endopeptidase Inhibitor
Chitin Binding
Transmembrane Transporter Activity
AP-2 Adaptor Complex Binding
Myosin Binding
Ser/Thr Kinase Activity
Transmembrane Transporter Binding
Small GTPase Binding
Cation Channel Activity
Protein Binding
ATP Binding
Zinc Ion Binding
Metallocarboxypeptidase Activity
Oxidoreductase Activity
RNA Pol II TF Activity
RNA Binding
Iron Ion Binding
CoA-Ligase Activity
Monooxygenase Activity
Glutathione Transferase Activity
d
Biological Process
Downregulated
Upregulated
Cilium Organization
Cellular Process
Non-Motile Cilium Assembly
Protein Localization to Cilium
Transmembrane Transport
NER, DNA Damage Recognition
UV-Damage Excision Repair
Base-Excision Repair
DNA Repair
Signal Transduction
Signaling
Regulation of DNA-Templated Transcription
Vesicle-Mediated Transport
mRNA Metabolic Process
DNA-Templated Transcription
Cellular Component
BBSome
Centrosome
Axoneme
Intracellular Anatomical Structure
Membrane
Microtubule Organizing Center
Cilium
Nucleotide-Excision Repair Factor 1 Complex
Chitin-Based Extracellular Matrix
Extracellular Matrix
Nucleus
Extracellular Region
Molecular Function
Patched Binding
Smoothened Binding
Damaged DNA Binding
Larval Cuticle Structural Constituent
Cuticle Structural Constituent
Structural Molecule Activity
3',5'-Cyclic-Nucleotide Phosphodiesterase Activity
Protein Binding
Histone Binding
Hydrolase Activity
ATP-Dependent Activity
DNA Binding
Isomerase Activity
Catalytic Activity, Acting on RNA

Figure 6

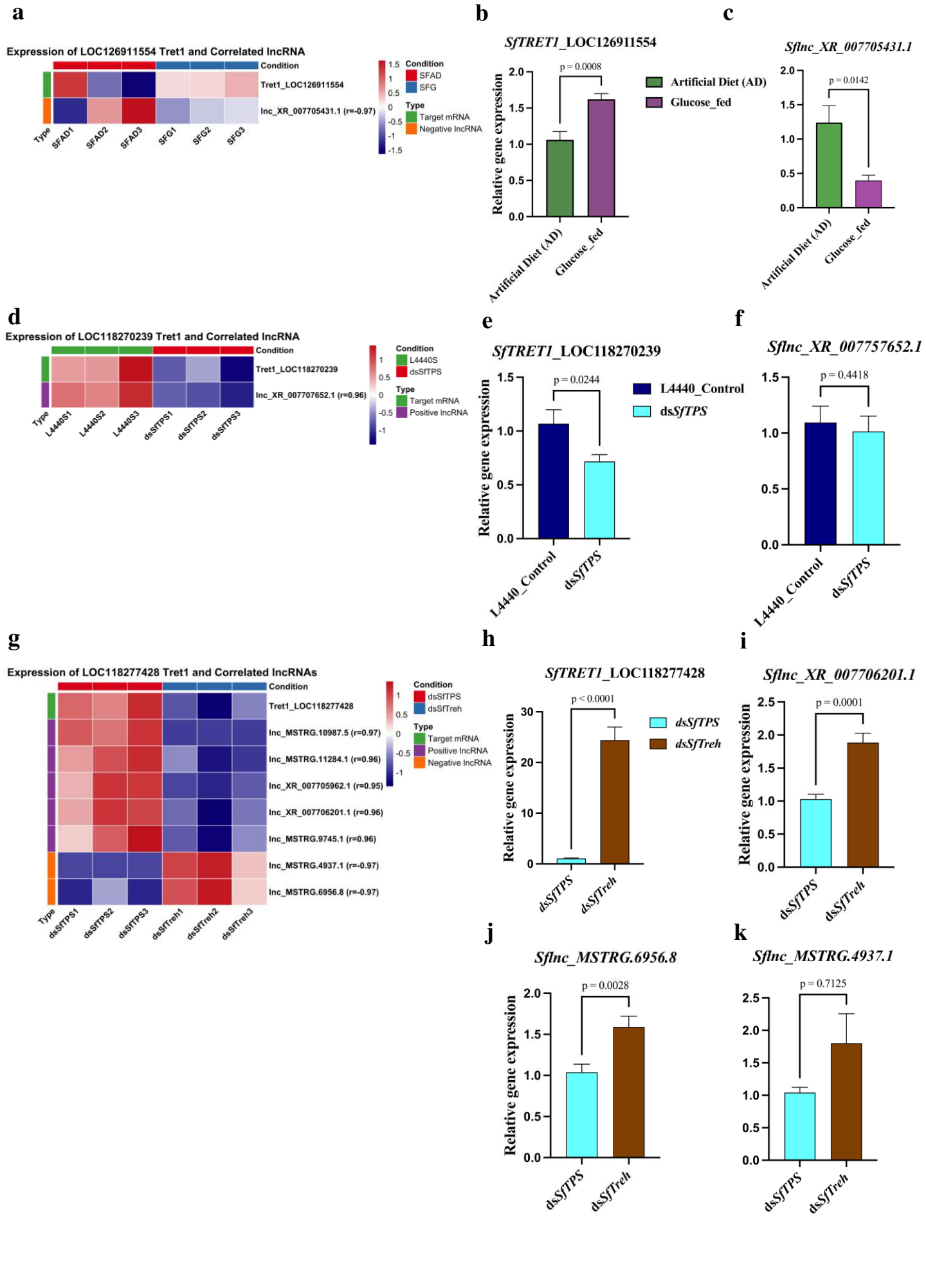

a
Expression of LOC126911554 Tret1 and Correlated lncRNA
Condition
Tret1_LOC126911554
lnc_XR_007705431.1 (r=-0.97)
Type
SFAD1
SFAD2
SFAD3
SFG1
SFG2
SFG3
Condition
SFAD
SFG
Type
Target mRNA
Negative lncRNA
b
SfTRET1_LOC126911554
p = 0.0008
Relative gene expression
Artificial Diet (AD)
Glucose_fed
c
Sflnc_XR_007705431.1
p = 0.0142
d
Expression of LOC118270239 Tret1 and Correlated lncRNA
Tret1_LOC118270239
lnc_XR_007707652.1 (r=0.96)
L4440S1
L4440S2
L4440S3
dsSfTPS1
dsSfTPS2
dsSfTPS3
L4440S
dsSfTPS
Positive lncRNA
e
SfTRET1_LOC118270239
p = 0.0244
L4440_Control
dsSfTPS
f
Sflnc_XR_007757652.1
p = 0.4418
g
Expression of LOC118277428 Tret1 and Correlated lncRNAs
Tret1_LOC118277428
lnc_MSTRG.10987.5 (r=0.97)
lnc_MSTRG.11284.1 (r=0.96)
lnc_XR_007705962.1 (r=0.95)
lnc_XR_007706201.1 (r=0.96)
lnc_MSTRG.9745.1 (r=0.96)
lnc_MSTRG.4937.1 (r=-0.97)
lnc_MSTRG.6956.8 (r=-0.97)
dsSfTPS1
dsSfTPS2
dsSfTPS3
dsSfTreh1
dsSfTreh2
dsSfTreh3
dsSfTPS
dsSfTreh
h
SfTRET1_LOC118277428
p < 0.0001
dsSfTPS
dsSfTreh
i
Sflnc_XR_007706201.1
p = 0.0001
j
Sflnc_MSTRG.6956.8
p = 0.0028
k
Sflnc_MSTRG.4937.1
p = 0.7125

Figure 7

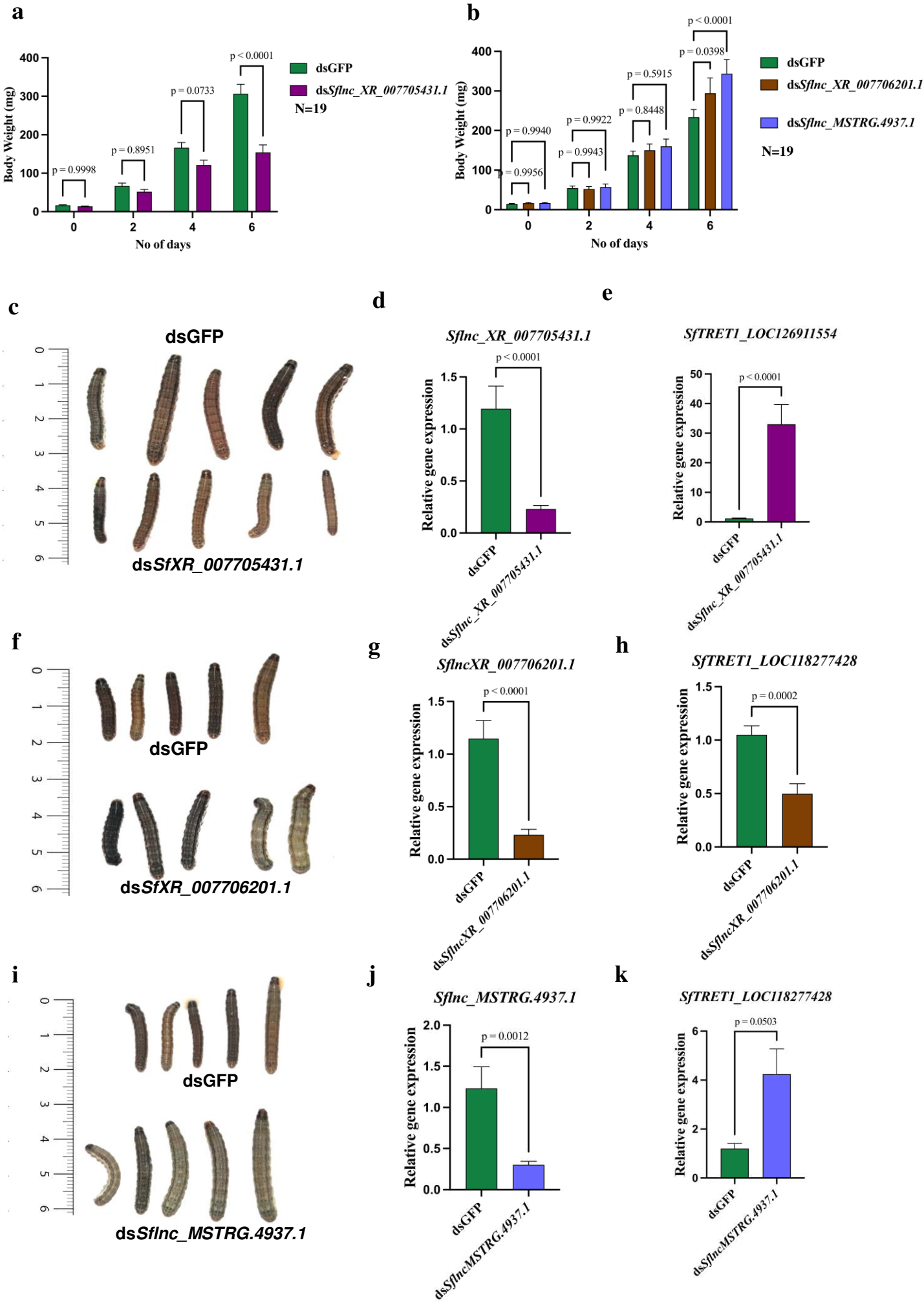
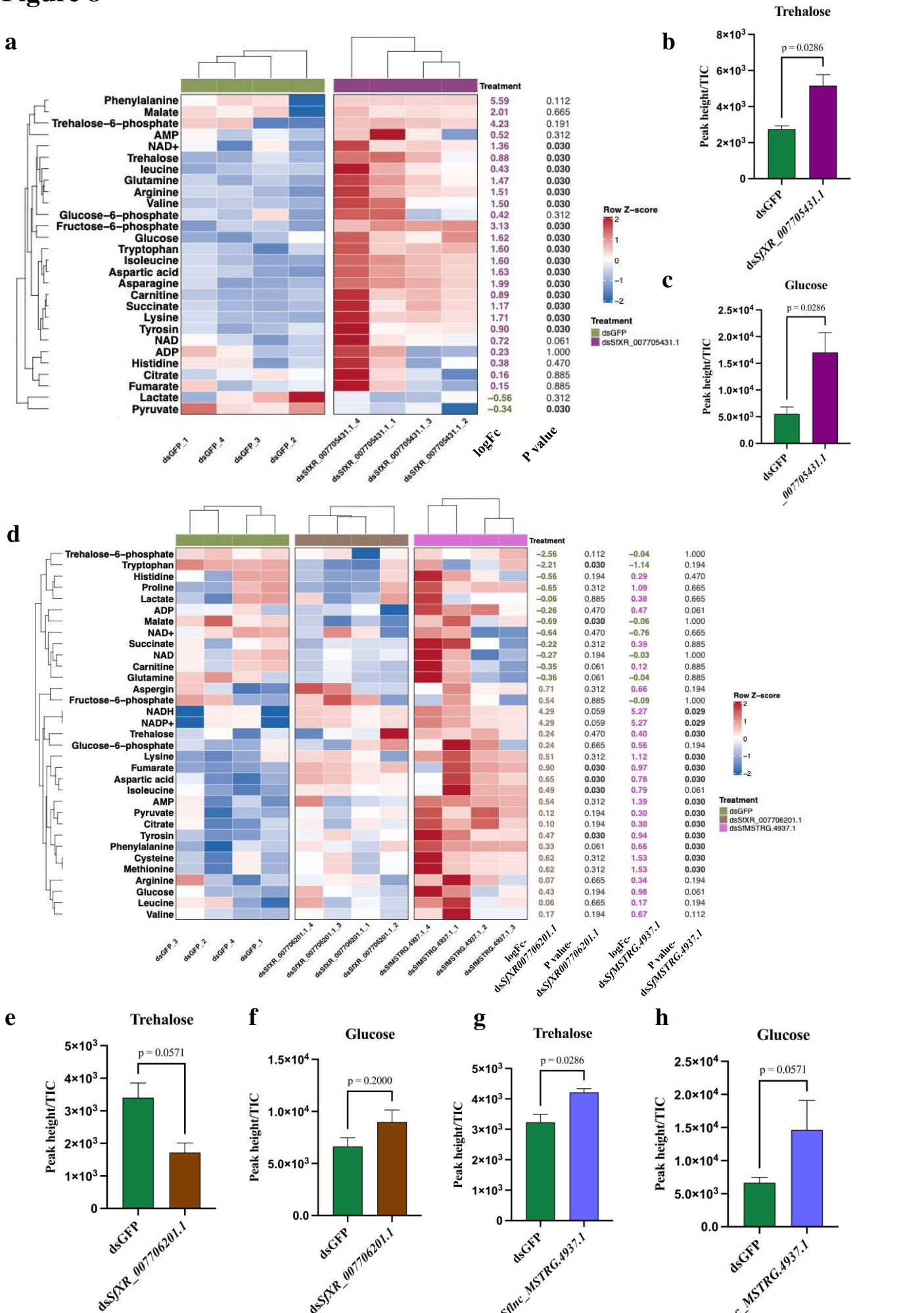

a
Body Weight (mg)
No of days
dsGFP
dsSflnc_XR_007705431.1
N=19
p = 0.9998
p = 0.8951
p = 0.0733
p < 0.0001
b
Body Weight (mg)
No of days
dsGFP
dsSflnc_XR_007706201.1
dsSflnc_MSTRG.4937.1
N=19
p = 0.9956
p = 0.9940
p = 0.9943
p = 0.9922
p = 0.8448
p = 0.5915
p = 0.0398
p < 0.0001
c
dsGFP
dsSfXR_007705431.1
d
Sflnc_XR_007705431.1
Relative gene expression
p < 0.0001
dsGFP
dsSflnc_XR_007705431.1
e
SfTRET1_LOC126911554
Relative gene expression
p < 0.0001
dsGFP
dsSflnc_XR_007705431.1
f
dsGFP
dsSfXR_007706201.1
g
SflncXR_007706201.1
Relative gene expression
p < 0.0001
dsGFP
dsSflncXR_007706201.1
h
SfTRET1_LOC118277428
Relative gene expression
p = 0.0002
dsGFP
dsSflncXR_007706201.1
i
dsGFP
dsSflnc_MSTRG.4937.1
j
Sflnc_MSTRG.4937.1
Relative gene expression
p = 0.0012
dsGFP
dsSflncMSTRG.4937.1
k
SfTRET1_LOC118277428
Relative gene expression
p = 0.0503
dsGFP
dsSflncMSTRG.4937.1

Figure 8


a
Treatment
Phenylalanine
Malate
Trehalose−6−phosphate
AMP
NAD+
Trehalose
leucine
Glutamine
Arginine
Valine
Glucose−6−phosphate
Fructose−6−phosphate
Glucose
Tryptophan
Isoleucine
Aspartic acid
Asparagine
Carnitine
Succinate
Lysine
Tyrosin
NAD
ADP
Histidine
Citrate
Fumarate
Lactate
Pyruvate
5.59 0.112
2.01 0.665
4.23 0.191
0.52 0.312
1.36 0.030
0.88 0.030
0.43 0.030
1.47 0.030
1.51 0.030
1.50 0.030
0.42 0.312
3.13 0.030
1.62 0.030
1.60 0.030
1.60 0.030
1.63 0.030
1.99 0.030
0.89 0.030
1.17 0.030
1.71 0.030
0.90 0.030
0.72 0.061
0.23 1.000
0.38 0.470
0.16 0.885
0.15 0.885
−0.56 0.312
−0.34 0.030
dsGFP_1
dsGFP_4
dsGFP_3
dsGFP_2
dsSfXR_007705431.1_4
dsSfXR_007705431.1_1
dsSfXR_007705431.1_3
dsSfXR_007705431.1_2
logFc
P value
Row Z-score
2
1
0
−1
−2
Treatment
dsGFP
dsSfXR_007705431.1
b
Trehalose
Peak height/TIC
8×10³
6×10³
4×10³
2×10³
0
p = 0.0286
dsGFP
dsSfXR_007705431.1
c
Glucose
Peak height/TIC
2.5×10⁴
2.0×10⁴
1.5×10⁴
1.0×10⁴
5.0×10³
0.0
p = 0.0286
dsGFP
_007705431.1
d
Treatment
Trehalose−6−phosphate
Tryptophan
Histidine
Proline
Lactate
ADP
Malate
NAD+
Succinate
NAD
Carnitine
Glutamine
Aspergin
Fructose−6−phosphate
NADH
NADP+
Trehalose
Glucose−6−phosphate
Lysine
Fumarate
Aspartic acid
Isoleucine
AMP
Pyruvate
Citrate
Tyrosin
Phenylalanine
Cysteine
Methionine
Arginine
Glucose
Leucine
Valine
−2.56 0.112 −0.04 1.000
−2.21 0.030 −1.14 0.194
−0.56 0.194 0.29 0.470
−0.65 0.312 1.09 0.665
−0.06 0.885 0.38 0.665
−0.26 0.470 0.47 0.061
−0.69 0.030 −0.06 1.000
−0.64 0.470 −0.76 0.665
−0.22 0.312 0.39 0.885
−0.27 0.194 −0.03 1.000
−0.35 0.061 0.12 0.885
−0.36 0.061 −0.04 0.885
0.71 0.312 0.66 0.194
0.54 0.885 −0.09 1.000
4.29 0.059 5.27 0.029
4.29 0.059 5.27 0.029
0.24 0.470 0.40 0.030
0.24 0.665 0.56 0.194
0.51 0.312 1.12 0.030
0.90 0.030 0.97 0.030
0.65 0.030 0.78 0.030
0.49 0.030 0.79 0.061
0.54 0.312 1.39 0.030
0.12 0.194 0.30 0.030
0.10 0.194 0.30 0.030
0.47 0.030 0.94 0.030
0.33 0.061 0.66 0.030
0.62 0.312 1.53 0.030
0.62 0.312 1.53 0.030
0.07 0.665 0.34 0.194
0.43 0.194 0.98 0.061
0.06 0.665 0.17 0.194
0.17 0.194 0.67 0.112
dsGFP_3
dsGFP_2
dsGFP_4
dsGFP_1
dsSfXR_007706201.1_4
dsSfXR_007706201.1_3
dsSfXR_007706201.1_1
dsSfXR_007706201.1_2
dsSfMSTRG.4937.1_4
dsSfMSTRG.4937.1_1
dsSfMSTRG.4937.1_2
dsSfMSTRG.4937.1_3
logFc-dsSfXR007706201.1
P value-dsSfXR007706201.1
logFc-dsSfMSTRG.4937.1
P value-dsSfMSTRG.4937.1
Row Z-score
2
1
0
−1
−2
Treatment
dsGFP
dsSfXR_007706201.1
dsSfMSTRG.4937.1
e
Trehalose
Peak height/TIC
5×10³
4×10³
3×10³
2×10³
1×10³
0
p = 0.0571
dsGFP
dsSfXR_007706201.1
f
Glucose
Peak height/TIC
1.5×10⁴
1.0×10⁴
5.0×10³
0.0
p = 0.2000
dsGFP
dsSfXR_007706201.1
g
Trehalose
Peak height/TIC
5×10³
4×10³
3×10³
2×10³
1×10³
0
p = 0.0286
dsGFP
dsSflnc_MSTRG.4937.1
h
Glucose
Peak height/TIC
2.5×10⁴
2.0×10⁴
1.5×10⁴
1.0×10⁴
5.0×10³
0.0
p = 0.0571
dsGFP
dsSflnc_MSTRG.4937.1

Supplementary Files

This is a list of supplementary files associated with this preprint. Click to download.

- NichitetalSupplementaryDEGsTableS2.xlsx
- NichitetalSupplementaryDElncRNAsTableS1.xlsx
- NichitetalSupplementaryTableS3.docx
- NichitetalSupplimnetryFigureV3.pdf